Chapter 3

Investigation of Neutron Induced Reaction Cross-sections

This chapter presents the measurement of neutron induced cross-sections of ^{58}Ni(n, p)^{58}Co and $^{115}\mathrm{In}(\mathrm{n},\mathrm{n}')^{115\mathrm{m}}\mathrm{In}$ reactions using quasi-monoenergetic neutrons generated using $^{7}\mathrm{Li}(\mathrm{p},\mathrm{n})$ reaction. The measured cross-sections were analyzed in comparison with experimental data reported in previous studies, as well as various evaluated data libraries, including ENDF/B-VIII.0, JEFF-3.3, JENDL-4.0, and CENDL-3.2. Additionally, the results were compared to theoretical predictions obtained using the TALYS and EMPIRE codes. The cross-section values are reported along with their corresponding absolute uncertainties, determined through uncertainty propagation utilizing the covariance technique. The results presented in this chapter are of significant importance for for advanced reactor, nuclear medicine and precise neutron flux determination in activation analysis.

The work presented in this chapter has been published in following Peer-Reviewed Journals:
1. A. Hingu, S. Mukherjee, et. al., Chin. Phys. C, **48**, 2, (2024). (© IOP Publishing. Reproduced with permission. All rights reserved.) **(I.F.=3.6)**
2. A. Hingu, B. Soni, et. al., Radiat. Phys. Chem., **199**, 110270, (2022). (According to the copyright agreement, the author retains the right to reuse the published work here as a part of this thesis.) (Elsevier Copyright Policy) **(I.F.=2.8)**

3.1 Introduction

The importance of neutron-induced reaction cross-section data lies in the advancement of the ongoing development of reactor technologies such as the ITER [1] and ADSs [2]. Accurate reaction cross-section data play a vital role in dose estimation and the discovery of innovative and economically efficient methods for synthesizing rare medical isotopes.

Exploring the uncertainty associated with the activation cross-section is crucial in determining the reasonable margin that ensures both economy and safety in nuclear reactor applications [3]. If multiple data points of the activation cross-sections are involved when evaluating the quantity of interest, the correlation (covariance) among the data points must also be examined to prevent overestimating or underestimating the uncertainty. Therefore, the aim of modern evaluation reports is not only to estimate the most accurate cross-section but also to identify the uncertainty and covariance describing the correlation among the cross-sections. However, in most previous data, details regarding error propagation and correlations among the different attributes are not reported. Considering the above facts, new experimental cross-sections with covariance analysis are needed to enhance the accuracy and reliability of these evaluated nuclear data and theoretical models.

This chapter focus on the precises measurement of neutron-induced reaction cross-sections for two specific reactions: ^{58}Ni(n, p)^{58}Co and ^{115}In(n, n')^{115m}In with covariance analysis. These measurements were performed using quasi-monoenergetic neutrons generated from the ^{7}Li(p, n) reaction, covering a range of incident neutron energies from 1.7 to 2.7 MeV and from 7 to 20 MeV, respectively. This chapter provides a systematic account of the experimental process, beginning with a comprehensive overview of the particle accelerator employed in the measurements. Subsequently, it delves into the mathematical description of the reaction cross-sections and elucidates the methodology employed for uncertainty propagation via covariance analysis. Further details regarding the experimental setup, data acquisition, and subsequent analysis are elaborated upon in later sections, offering a deeper understanding of the observed results and their implications.

3.2 Neutron Generation Facility

Accelerators stand as the primary neutron production facility, renowned for their capacity to generate high-intensity neutron beams. In this context, charged particle accelerators are essential for generating secondary neutron beams.. The specific charged particle-based neutron facilities employed in the current study are (1) FOTIA Accelerator Facility [4, 5] and (2) 14UD Pelletron Accelerator Facility [6]. The ensuing section provides a comprehensive overview of each facility.

3.2.1 FOTIA Accelerator Facility

The FOTIA (Folded Tandem Ion Accelerator) facility, located at the Bhabha Atomic Research Centre (BARC) in Mumbai, India represents a cutting-edge platform for ion acceleration and research. This facility features a Tandem Van de Graaff type electrostatic accelerator with a maximum terminal voltage of 6 MV. Developed indigenously by BARC, the FOTIA accelerator is versatile, capable of accelerating ions across a range of charge states, from hydrogen to heavy uranium. A schematic diagram of FOTIA accelerator facility is shown in Fig. (3.1).

In FOTIA, negative ions are generated by a state-of-the-art Source of Negative Ions by Cesium Sputtering-II (SNICS-II) ion source. at an initial energy of 150 keV. The ions are then introduced into the low-energy accelerating tube, where they undergo acceleration up to a maximum energy of 6 MeV. Upon reaching the high-voltage terminal, the negative ions undergo a sophisticated charge conversion process, wherein they are stripped of their electrons to become positively charged ions. This conversion is facilitated by advanced charge stripping techniques integrated into the terminal setup. The positively charged ions are subsequently deflected by an 180° magnet positioned within the high-voltage terminal, ensuring precise control and trajectory alignment. Subsequently, the ion beam is directed into the second accelerating tube, seamlessly integrated within the same column section. Here, ions undergo an additional energy gain of neV, contributing to a total energy output of (1+n) eV MeV. In this expression, "V" represents the terminal voltage, and "n" signifies the charge state of the ions. To ensure accurate analysis of the ion beam energy, sophisticated beam diagnostics tools are employed, including a high-resolution 90° magnet. This enables FOTIA to achieve an exceptional energy resolution of 2 keV, facilitating precise characterization and manipulation of ion energies. The versatility and precision offered by the FOTIA facility make it an indispensable resource for a wide range of scientific investigations, from fundamental particle physics to practical applications in nuclear physics, materials science, and beyond.

3.2.2 14UD Pelletron Accelerator Facility

The 14UD Pelletron Accelerator at the Tata Institute of Fundamental Research (TIFR) in Mumbai, India utilizes a unique charging mechanism ("Pelletron" from "pellet"), employing a chain of small metal pellets (1" × 1.5") linked by nylon instead of the conventional belt found in standard Van de Graaff accelerators. This tandem electrostatic accelerator propels charged particles to high energies through multiple stages of acceleration. Based on the tandem acceleration principle, it initially strips electrons from the ions, followed by further acceleration through successive voltage stages. This efficient approach enables the attainment of desired particle energies for various experimental applications in fields such as nuclear physics, materials science, and particle therapy. The innovative

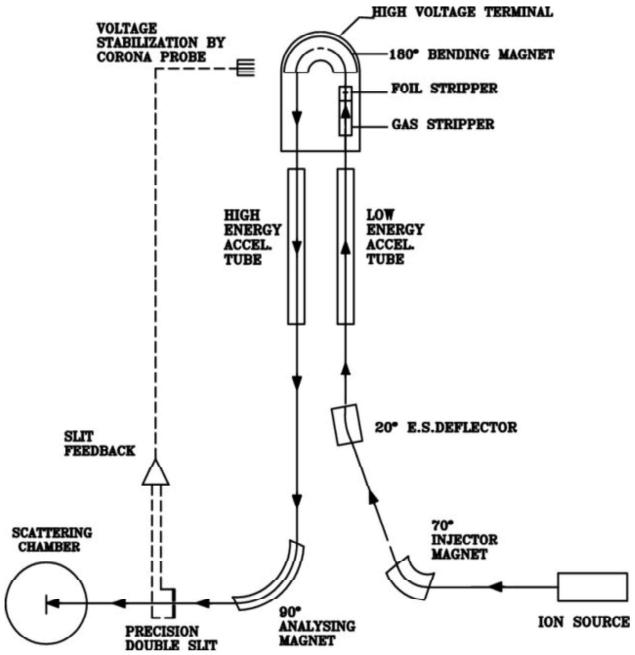

Fig. 3.1: Diagrammatic representation of FOTIA accelerator Facility.

design transports the charge to the terminal, raising its potential to 14 MV. The accelerating tube, composed of demountable ceramic insulator sections and titanium metal electrodes, spans a vertical height of 150 ft. The central terminal, reaching a potential of 14 MV with a stability of +2 kV, distributes this potential across 14 sections of the accelerating tube on each side. A typical schematic diagram of Pelletron setup is illustrated in Fig. (3.2).

The ion source, located atop the accelerator tower, utilizes a cesium sputter ion-source to generate negative ions from a selected source. These negative ions, initially accelerated to energies of approximately 300 keV, are then injected into the main beam pipe of the Pelletron through an injector magnet. To ensure insulation between the steel tank walls and the accelerator tank, $\mathrm{SF_6}$ gas—a highly insulating medium—is employed. This prevents any short-circuiting between the Pelletron and the tank walls. The beam is subsequently directed to the high positive potential terminal, $\mathrm{V_t}$, positioned at the center of the tank, where the ions' energy is further increased to $\mathrm{qV_t}$. Continuous charge transfer to the terminal, facilitated by a rotating chain of steel pellets, maintains the high electric potential. Within the terminal, ions pass through a thin carbon foil or a small volume of gas, known as a stripper, where they lose electrons and become highly positive. As the terminal maintains a high positive potential, the positively charged ions experience repulsion and accelerate towards the bottom of the tank, which is grounded. Finally, the accelerated ion-beam can be directed to any desired beam-line within the main beam hall of the BARC-TIFR facility using switching magnets. After passing through the stripper, if the charge state of positive ions is "q", their final energy after acceleration to the base of the tank

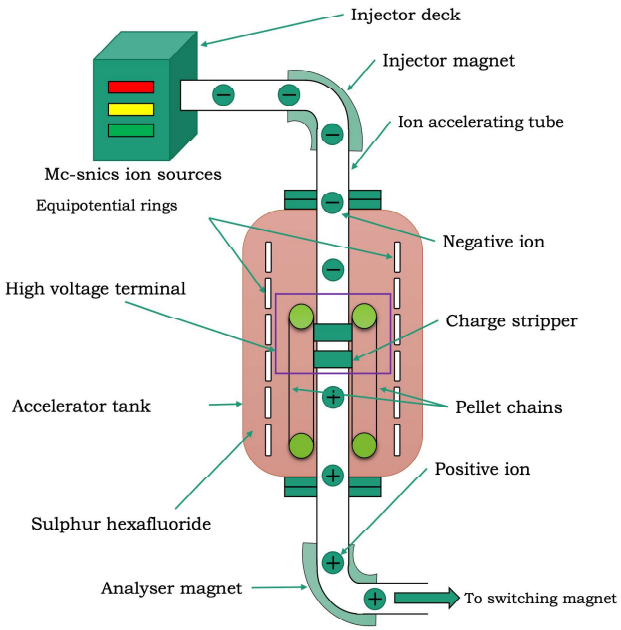

Fig. 3.2: Diagrammatic representation of 14UD Pelletron Accelerator installed at BARC-TIFR Facility.

is given by:

$$\mathrm{E_{fin}} = \mathrm{E_{int}} + (\mathrm{q}+1)\mathrm{V_t}. \tag{3.1}$$

Here, $\mathrm{E_{int}}$ is the initial energy of ions from the ion-source, and "q" represents the charge state after stripping. This equation summarizes the relationship between initial energy, charge state, and additional energy gained during acceleration.

In current study, both accelerators were extensively utilized to generate neutron beams at different projectile energies. Neutrons were produced via $^{7}\mathrm{Li}(\mathrm{p},\mathrm{n})$ reaction, with energy ranges of 1.7-2.7 MeV from FOTIA and 7-20 MeV from the Pelletron accelerator. Detailed procedures for neutron-induced reactions are outlined in Sections 3.5.1 and 3.6.1.

3.3 Reaction Cross-section: Mathematical Formulation

Nuclear reactions generally take place when a sample is irradiated with a particle beam, leading to the creation of a compound nucleus, followed by subsequent decay processes that yield reaction residues, releasing particles such as protons, neutrons, γ-rays, and α particles. These residual nuclei exist in excited states and often transition to the ground state through the emission of characteristic γ-rays. In the specific nuclear reaction $\mathrm{X}(\mathrm{x},\mathrm{y})\mathrm{Y}$, where a projectile particle x collides with the target nucleus X, transmutation occurs, resulting in the creation of a new nucleus Y and the emission of an ejectile particle y. To characterize

the activation process, it is crucial to quantify the initial number of populated residues. Denoting the initial number of nuclei in the target as $\mathrm{N_0}$, the neutron flux as Φ, and the activation cross-section for the target nuclei in a specific reaction channel as σ, the no. of Y nuclei produced in time dt is equal to the no. of X nuclei transmuted as a result of above reaction, which is determined by the expression:

$$\mathrm{dN_Y} = \sigma\ \mathrm{N_0}\ \Phi\ \mathrm{dt}. \tag{3.2}$$

The no. of Y nuclei produced over time t is provided by the integral,

$$\mathrm{N_Y} = \int_0^{\mathrm{t}} \mathrm{dN_Y} = \sigma\ \mathrm{N_0}\ \Phi\ \mathrm{t}. \tag{3.3}$$

If the produced nuclei Y are radioactive, with disintegration constant λ, then the rate of change of the no. of Y nuclei is equal to (rate of production- rate of disintegration),

$$\frac{\mathrm{dN_Y}}{\mathrm{dt}} = \sigma\ \mathrm{N_0}\ \Phi - \lambda\ \mathrm{N_Y}. \tag{3.4}$$

Solving this differential equation yields the following expression,

$$\mathrm{N_Y} - \frac{\sigma\ \mathrm{N_0}\ \Phi}{\lambda} = \mathrm{A}\ \mathrm{e}^{-\lambda \mathrm{t}}, \tag{3.5}$$

where A serves as an integration constant, specifically determined as,

$$\mathrm{A} = -\frac{\sigma\ \mathrm{N_0}\ \Phi}{\lambda}. \tag{3.6}$$

The yield of nuclei Y produced during the irradiation time $\mathrm{t_i}$ is given by,

$$\mathrm{N_Y(t_i)} = \frac{\sigma\ \mathrm{N_0}\ \Phi}{\lambda}(1 - \mathrm{e}^{-\lambda \mathrm{t_i}}). \tag{3.7}$$

The no. of Y nuclei left in the sample after cooling time $\mathrm{t_w}$ from end of the bombardment of foil is given by,

$$\mathrm{N_Y(t_w)} = \mathrm{N_Y(t_i)}\ \mathrm{e}^{-\lambda \mathrm{t_w}}, \tag{3.8}$$

$$\mathrm{N_Y(t_w)} = \frac{\sigma\ \mathrm{N_0}\ \Phi}{\lambda}(1 - \mathrm{e}^{-\lambda \mathrm{t_i}})\ \mathrm{e}^{-\lambda \mathrm{t_w}}. \tag{3.9}$$

Its radioactivity at this instant is given by,

$$\frac{\mathrm{dN_Y(t_w)}}{\mathrm{dt_w}} = \lambda \mathrm{N_Y(t_w)}, \tag{3.10}$$

$$\frac{\mathrm{dN_Y(t_w)}}{\mathrm{dt_w}} = \sigma\ \mathrm{N_0}\ \Phi(1 - \mathrm{e}^{-\lambda \mathrm{t_i}})\ \mathrm{e}^{-\lambda \mathrm{t_w}}. \tag{3.11}$$

If it is at safe level then only do the counting of the sample. Now no. of Y nuclei left in counting time t_c is,

$$N_Y(t_c) = N_Y(t_w)e^{-\lambda t_c}, \tag{3.12}$$

$$N_Y(t_c) = \frac{\sigma\, N_0\, \Phi}{\lambda}(1-e^{-\lambda t_i})\; e^{-\lambda t_w} e^{-\lambda t_c}. \tag{3.13}$$

This gives the no. of counts in given counting time t_c. No. of Y nuclei disintegrated in cooling time t_w is,

$$N_Y(t_i) - N_Y(t_w) = \frac{\sigma\, N_0\, \Phi}{\lambda}(1-e^{-\lambda t_i})\; (1-e^{-\lambda t_w}). \tag{3.14}$$

No. of Y nuclei disintegrated in counting time t_c is,

$$N_Y(t_w) - N_Y(t_c) = \frac{\sigma\, N_0\, \Phi}{\lambda}(1-e^{-\lambda t_i})\; e^{-\lambda t_w}\; (1-e^{-\lambda t_c}). \tag{3.15}$$

This is the total count we will get from the disintegration of nuclei Y. Now due to detector efficiency(ε) and branching intensity, the total count is converted to observed count (A_γ) which is given by,

$$A_\gamma = \frac{\sigma\, N_0\, \Phi\, \varepsilon\, I_\gamma}{\lambda}(1-e^{-\lambda t_i})\; e^{-\lambda t_w}\; (1-e^{-\lambda t_c}). \tag{3.16}$$

The reaction cross-section can be written as,

$$\sigma = \frac{A_\gamma\, \lambda}{N_0\, \Phi\, \varepsilon\, I_\gamma\, (1-e^{-\lambda t_i})\, e^{-\lambda t_w}\, (1-e^{-\lambda t_c})}, \tag{3.17}$$

where, A_γ represents the count within the photo-peak of the characteristic γ-ray. Eq. (3.17) is utilized to compute the reaction cross-section of a residue at a specified energy. Given potential variations between the detector's counting time (t_c) and the actual counting time (t_r) caused by detector dead time, it is advisable to consider a modification to previous equation,

$$\sigma = \frac{A_\gamma\, \lambda\, \left(\frac{t_c}{t_r}\right)}{N_0\, \Phi\, \varepsilon\, I_\gamma\, (1-e^{-\lambda t_i})\, e^{-\lambda t_w}\, (1-e^{-\lambda t_c})}, \tag{3.18}$$

where,

A_γ = characteristic γ-ray photo-peak counts for the product nuclide;
λ = decay constant (s^{-1});
t_i = irradiation time (s);
t_c = counting time (s);
t_w = cooling time (s);
t_r = real time (clock time) (s);
N_0 = total number of target nuclei in the sample;
I_γ = branching intensity of γ-ray [7];
ε = detector efficiency.

In the context of neutron-induced reactions, measuring neutron flux directly is not possible. Consequently, a monitor reaction was employed in each case to calculate the neutron flux, utilizing either evaluated or experimental cross-sections as the principal input for the monitor reaction. The neutron flux ($\langle\Phi\rangle$) can be written as,

$$\langle\Phi\rangle = \frac{\mathrm{A}_\gamma\ \lambda\ \left(\frac{\mathrm{t_c}}{\mathrm{t_r}}\right)}{\mathrm{N}_0\ \langle\sigma_\mathrm{m}\rangle\ \varepsilon\ \mathrm{I}_\gamma\ \left(1-\mathrm{e}^{-\lambda \mathrm{t_i}}\right)\ \mathrm{e}^{-\lambda \mathrm{t_w}}\ \left(1-\mathrm{e}^{-\lambda \mathrm{t_c}}\right)}, \tag{3.19}$$

where, $\langle\sigma_\mathrm{m}\rangle$ refers to a spectral weighted cross-section for the monitor reaction and the meanings of all other symbols are related to those specified in Eq. (3.18). Hence, the cross-section σ_R for the neutron-induced reaction can be expressed by utilizing Eqs. (3.18) and (3.19) as,

$$\sigma_\mathrm{R} = \frac{\mathrm{A}_\gamma\ \lambda\ \left(\frac{\mathrm{t_c}}{\mathrm{t_r}}\right)}{\mathrm{N}_0\ \langle\Phi\rangle\ \varepsilon\ \mathrm{I}_\gamma\ \left(1-\mathrm{e}^{-\lambda \mathrm{t_i}}\right)\ \mathrm{e}^{-\lambda \mathrm{t_w}}\ \left(1-\mathrm{e}^{-\lambda \mathrm{t_c}}\right)}. \tag{3.20}$$

Indirect neutron flux calculations may result in considerable uncertainties and strong correlations among measured quantities. To address this in neutron-induced reaction cross-sections, uncertainties are assessed using widely accepted covariance analysis [8, 9]. This method, recommended for precise data evaluations, is detailed in the following section.

3.4 Uncertainty Propagation via Covariance Analysis

The accuracy of the data depends not solely on the measured values but also on their associated uncertainties. Ideally, we aim to understand all potential sources of uncertainty during both the experiment and data processing stages. However, having this knowledge alone is not enough; we also need to analyze how and where the uncertainties propagate.

Covariance analysis is a statistical and mathematical method based on error estimates that gives the reliable estimate of uncertainty as well as cross-correlations among the observable values, specifically the reaction cross-sections in this context. Apart from the counting statistics from a spectrum, other quantities like, efficiency of detector, γ-abundances, half-life of residues, flux etc are obtained from various sources and may involve significant uncertainty. Consequently, by employing this method, we can effectively incorporate the errors from all sources into the final measured values of the cross-sections.

The technique relies on the assumption that when we observe something, the result can be thought of as a random variable, like a list of values $\mathrm{x} = (\mathrm{x}_1, \mathrm{x}_2, \mathrm{x}_3, ..., \mathrm{x}_\mathrm{n})$. The normalization requirement for the probability distribution $\mathrm{p(x)}$ of x can be expressed as, $\int_{-\infty}^{\infty} \mathrm{p(x)dx}$=1, where $\mathrm{dx} = \mathrm{dx}_1, \mathrm{dx}_2, \mathrm{dx}_3, ..., \mathrm{dx}_\mathrm{n}$.

The expectation value "A" of a real-valued function $f(x)$ can be expressed as,

$$A(f(x)) = \int_{-\infty}^{\infty} f(x)\ p(x)\ dx. \tag{3.21}$$

The mean and variance of variable x_k are given as,

$$\tilde{x}_k = A(x_k); Var(x_k) = A[(x_k - \tilde{x}_k)^2]. \tag{3.22}$$

As the variables are dependent, the covariance and correlation among the variables x_k are defined as [9],

$$Cov(x_k, x_i) = \int (x_k - \tilde{x}_k)\ (x_i - \tilde{x}_i)\ p(x_1, x_2, x_3, ..., x_n)\ dx, \tag{3.23}$$

$$Corr(x_k, x_i) = \frac{Cov(x_k, x_i)}{\sqrt{Var(x_k)}\ \sqrt{Var(x_i)}}, \tag{3.24}$$

where, $-1 \leq Corr(x_k, x_i) \leq 1$ and the uncertainty can be defined as the standard deviation $\Delta x_k = \sqrt{Var(x_k)}$.

3.4.1 Uncertainty in the Efficiency of HPGe Detector

The efficiency calibration of the HPGe detector was performed with a ^{152}Eu standard multi-gamma point source using following Eq:

$$\varepsilon_p = K_f\ \frac{C}{A_0\ I_\gamma\ e^{-\lambda T}\ \Delta t}. \tag{3.25}$$

In this context, the symbol A_0 denotes the activity of the ^{152}Eu point source at the time of its production. The total number of counts recorded for a specific γ-ray energy, along with its absolute intensity (I_γ) over a counting period, is represented by C. The decay constant is denoted by λ, while the elapsed time between the production and counting dates is referred to as T. The coincidence summing correcting factor is abbreviated as K_f.

Various sources of uncertainty exist in the calibration process, from C, I_γ, A_0, and $t_{1/2}$, which propagate as the uncertainty in the detector's efficiency ("K_f" and "t" are considered constants without inherent uncertainty in the current measurement). Hence, a Taylor series expansion can be used to expand the detetor efficiency as a function of four attributes, $\varepsilon = f(C,\ I_\gamma,\ A_0,\ t_{1/2})$:

$$\Delta\varepsilon = \left(\frac{\partial\varepsilon}{\partial C}\right) \Delta C\ +\ \left(\frac{\partial\varepsilon}{\partial I_\gamma}\right) \Delta I_\gamma\ +\ \left(\frac{\partial\varepsilon}{\partial A_0}\right) \Delta A_0\ +\ \left(\frac{\partial\varepsilon}{\partial t_{1/2}}\right) \Delta t_{1/2}. \tag{3.26}$$

Squaring both sides of the equation and omitting higher-order terms yields,

$$(\Delta\varepsilon)^2 = \left(\frac{\partial\varepsilon}{\partial \mathrm{C}}\right)^2 (\Delta \mathrm{C})^2 + \left(\frac{\partial\varepsilon}{\partial \mathrm{I}_\gamma}\right)^2 (\Delta \mathrm{I}_\gamma)^2 + \left(\frac{\partial\varepsilon}{\partial \mathrm{A}_0}\right)^2 (\Delta \mathrm{A}_0)^2 + \left(\frac{\partial\varepsilon}{\partial \mathrm{t}_{1/2}}\right)^2 (\Delta \mathrm{t}_{1/2})^2 + 2\left(\frac{\partial\varepsilon}{\partial \mathrm{C}}\right)\left(\frac{\partial\varepsilon}{\partial \mathrm{I}_\gamma}\right)\mathrm{Cov}(\mathrm{C},\mathrm{I}_\gamma) + 2\left(\frac{\partial\varepsilon}{\partial \mathrm{C}}\right)\left(\frac{\partial\varepsilon}{\partial \mathrm{A}_0}\right)\mathrm{Cov}(\mathrm{C},\mathrm{A}_0) + 2\left(\frac{\partial\varepsilon}{\partial \mathrm{C}}\right)\left(\frac{\partial\varepsilon}{\partial \mathrm{t}_{1/2}}\right)\mathrm{Cov}(\mathrm{C},\mathrm{t}_{1/2}) + 2\left(\frac{\partial\varepsilon}{\partial \mathrm{I}_\gamma}\right)\left(\frac{\partial\varepsilon}{\partial \mathrm{A}_0}\right)\mathrm{Cov}(\mathrm{I}_\gamma,\mathrm{A}_0) + 2\left(\frac{\partial\varepsilon}{\partial \mathrm{I}_\gamma}\right)\left(\frac{\partial\varepsilon}{\partial \mathrm{t}_{1/2}}\right)\mathrm{Cov}(\mathrm{I}_\gamma,\mathrm{t}_{1/2}) + 2\left(\frac{\partial\varepsilon}{\partial \mathrm{A}_0}\right)\left(\frac{\partial\varepsilon}{\partial \mathrm{t}_{1/2}}\right)\mathrm{Cov}(\mathrm{A}_0,\mathrm{t}_{1/2}). \tag{3.27}$$

$$(\Delta\varepsilon)^2 = \begin{bmatrix}\left(\frac{\partial\varepsilon}{\partial \mathrm{C}}\right) & \left(\frac{\partial\varepsilon}{\partial \mathrm{I}_\gamma}\right) & \left(\frac{\partial\varepsilon}{\partial \mathrm{A}_0}\right) & \left(\frac{\partial\varepsilon}{\partial \mathrm{t}_{1/2}}\right)\end{bmatrix} \begin{bmatrix} (\Delta \mathrm{C})^2 & \mathrm{Cov}(\mathrm{C},\mathrm{I}_\gamma) & \mathrm{Cov}(\mathrm{C},\mathrm{A}_0) & \mathrm{Cov}(\mathrm{C},\mathrm{t}_{1/2}) \\ \mathrm{Cov}(\mathrm{C},\mathrm{I}_\gamma) & (\Delta \mathrm{I}_\gamma)^2 & \mathrm{Cov}(\mathrm{I}_\gamma,\mathrm{A}_0) & \mathrm{Cov}(\mathrm{I}_\gamma,\mathrm{t}_{1/2}) \\ \mathrm{Cov}(\mathrm{C},\mathrm{A}_0) & \mathrm{Cov}(\mathrm{I}_\gamma,\mathrm{A}_0) & (\Delta \mathrm{A}_0)^2 & \mathrm{Cov}(\mathrm{A}_0,\mathrm{t}_{1/2}) \\ \mathrm{Cov}(\mathrm{C},\mathrm{t}_{1/2}) & \mathrm{Cov}(\mathrm{I}_\gamma,\mathrm{t}_{1/2}) & \mathrm{Cov}(\mathrm{A}_0,\mathrm{t}_{1/2}) & (\Delta \mathrm{t}_{1/2})^2 \end{bmatrix} \begin{bmatrix}\left(\frac{\partial\varepsilon}{\partial \mathrm{C}}\right) \\ \left(\frac{\partial\varepsilon}{\partial \mathrm{I}_\gamma}\right) \\ \left(\frac{\partial\varepsilon}{\partial \mathrm{A}_0}\right) \\ \left(\frac{\partial\varepsilon}{\partial \mathrm{t}_{1/2}}\right)\end{bmatrix}. \tag{3.28}$$

Since the measured attributes C, I_γ, A_0, and $\mathrm{t}_{1/2}$ are uncorrelated, the uncertainty in the detector efficiency can be determined using the quadratic sum formula for i gamma lines as,

$$(\Delta\varepsilon)^2 = \left(\frac{\partial\varepsilon}{\partial \mathrm{C}}\right)^2 (\Delta \mathrm{C})^2 + \left(\frac{\partial\varepsilon}{\partial \mathrm{I}_\gamma}\right)^2 (\Delta \mathrm{I}_\gamma)^2 + \left(\frac{\partial\varepsilon}{\partial \mathrm{A}_0}\right)^2 (\Delta \mathrm{A}_0)^2 + \left(\frac{\partial\varepsilon}{\partial \mathrm{t}_{1/2}}\right)^2 (\Delta \mathrm{t}_{1/2})^2. \tag{3.29}$$

This can be written as:

$$\left(\frac{\Delta\varepsilon_\mathrm{i}}{\varepsilon_\mathrm{i}}\right)^2 = \left(\frac{\Delta \mathrm{C_i}}{\mathrm{C_i}}\right)^2 + \left(\frac{\Delta \mathrm{I}_{\gamma_\mathrm{i}}}{\mathrm{I}_{\gamma_\mathrm{i}}}\right)^2 + \left(\frac{\Delta \mathrm{A}_{0_\mathrm{i}}}{\mathrm{A}_{0_\mathrm{i}}}\right)^2 + \left(\mathrm{T}\ln 2\,\frac{\Delta \mathrm{t}_{1/2}}{\mathrm{t}_{1/2}^2}\right)^2, \tag{3.30}$$

where the terms are defined as in Reference [8]. The covariance matrix for detector efficiencies can now be constructed using,

$$(\mathrm{V}_\varepsilon)_{\mathrm{ij}} = \sum_\mathrm{r} \mathrm{e_{ir}}\ \mathrm{S_{ijr}}\ \mathrm{e_{jr}}, \tag{3.31}$$

where $\mathrm{e_{ir}}$ and $\mathrm{e_{jr}}$ are the diagonal matrices, whereas $\mathrm{S_{ijr}}$ denotes the micro-correlation matrices. $\mathrm{S_{ijr}}$ may be expressed as an $(\mathrm{n}\times\mathrm{n})$ unity matrix for the uncorrelated and as a square matrix of order $(\mathrm{n}\times\mathrm{n})$ with each element set to "1" for the fully correlated case. For partially correlated cases, $\mathrm{S_{ijr}}$ can also be an $(\mathrm{n}\times\mathrm{n})$ matrix with elements $0 < \mathrm{S_{ijr}} < 1$.

- The counts (C) from different γ-ray lines are uncorrelated, as they are independently measured. Therefore $\mathrm{S_{ijr}}$ for counts will be an identity matrix.
- The γ-ray abundances (I_γ) for each line are also uncorrelated because they are specific to each line and hence they are also taken as uncorrelated.
- The initial activity (A_0) is correlated as it is common to all lines. The $\mathrm{S_{ijr}}$ matrix in this particular case would be a square matrix.

- Since all lines share the same half-life ($t_{1/2}$) and originate from the same radioactive decay process, they exhibit a correlation in their decay behavior.

  The S_{ijr} for C, I_γ, A_0, and $t_{1/2}$ can be designated as,

$$\begin{pmatrix} 1 & 0 & \cdots & 0 \\ 0 & 1 & \cdots & 0 \\ \vdots & \vdots & \ddots & \vdots \\ 0 & 0 & \cdots & 1 \end{pmatrix}, \begin{pmatrix} 1 & 1 & \cdots & 1 \\ 1 & 1 & \cdots & 1 \\ \vdots & \vdots & \ddots & \vdots \\ 1 & 1 & \cdots & 1 \end{pmatrix}, \begin{pmatrix} 1 & 0 & \cdots & 0 \\ 0 & 1 & \cdots & 0 \\ \vdots & \vdots & \ddots & \vdots \\ 0 & 0 & \cdots & 1 \end{pmatrix} \& \begin{pmatrix} 1 & 1 & \cdots & 1 \\ 1 & 1 & \cdots & 1 \\ \vdots & \vdots & \ddots & \vdots \\ 1 & 1 & \cdots & 1 \end{pmatrix}.$$

The γ-rays used in the calculations (say E_i) may differ from those utilized in the efficiency calculations.. Hence the detector efficiencies for the γ-lines E_i can be calculated using the model interpolation [8],

$$\ln \varepsilon_i = \sum_m p_m \, (\ln E_i)^{m-1}, \tag{3.32}$$

where ε_i represents the efficiencies, p_m is the fitting parameter of order m, and E_i denotes the corresponding γ-ray energies. A linear model, $Z = AP$ may be used to solve Eq. (3.32). The column matrix of Z is determined by $z_i = \ln \varepsilon_i$. Matrix A is a design matrix where the elements are given by $A_{il} = (\ln E_i)^{l-1}$, while matrix P contains elements computed as p_m using the least squares method. The solution parameters were derived using the covariance matrix:

$$V_p = (A^{'} \, V_z^{-1} \, A)^{-1}. \tag{3.33}$$

The parameters p_m can now be evaluated as follows:

$$\hat{P} = V_{\hat{P}} \, (A^{'} \, V_z^{-1} \, Z), \tag{3.34}$$

where matrix V_z can be calculated by using the following equation:

$$(V_z)_{ij} = \frac{(V_\varepsilon)_{ij}}{\langle \epsilon_i \rangle \langle \epsilon_j \rangle}. \tag{3.35}$$

In the final step, the goodness of fit is calculated using Eq. (3.36),

$$\chi^2_m = (Z - AP)^{'} \, V_z^{-1} \, (Z - AP). \tag{3.36}$$

The above-mentioned calculations enable the determination of the covariance matrix for the cross-sections.

The fitting parameter obtained from the Eq. (3.32) can be used to calculate the efficiencies for the γ-lines of the sample and monitor reactions. The covariance matrix for new efficiencies can be calculated by utilizing matrices Z and A using following Eqs:

$$V_{z_{\varepsilon_i}} = A' \, V_{\hat{P}} \, A, \tag{3.37}$$

&

$$V_{\varepsilon_{ij}} = \varepsilon_i \, V_{z_{\varepsilon_i}} \, \varepsilon_j, \tag{3.38}$$

where $V_{z_{\varepsilon_i}}$ and $V_{\varepsilon_{ij}}$ denotes the covariance matrix for the column matrix Z and for the efficiencies of the sample and monitor γ-lines, respectively.

3.4.2 Uncertainty in the Reaction Cross-section Measurement

By using Eqs. (3.19) and (3.20), we can redefine Eq. (3.20) for the present reaction parameter (r) and the monitor reaction parameter (m) as the ratio measure technique [9] for the covariance analysis in activation cross-section measurement.

$$\langle \sigma_r \rangle \; = \; \langle \sigma_m \rangle \frac{C_r \, I_{\gamma m} \, \varepsilon_m \, f_{\lambda m}}{C_m \, I_{\gamma r} \, \varepsilon_r \, f_{\lambda r}}, \tag{3.39}$$

with the time factor f defined as,

$$f = \frac{(1 - e^{-\lambda t_i})(1 - e^{-\lambda t_c})(e^{-\lambda t_w})}{\lambda}. \tag{3.40}$$

The quadratic sum formula may be used to determine the uncertainty related to each attribute in Eq. (3.39). The attribute f contains five sources of uncertainty (t_i, t_c, t_w, λ_r and λ_m) out of all the attributes in Eq. (3.39). Here, the uncertainty in the decay constants (λ_r and λ_m) is related to the cross-section via the exponential function. Consequently, the uncertainty in decay constants (in terms of time factors) is defined as,

$$\left(\frac{\Delta f}{f}\right)^2 = s_{f\lambda}^2 \left(\frac{\Delta \lambda}{\lambda}\right)^2, \tag{3.41}$$

where, $\Delta\lambda \; = \; (\ln 2 \; \Delta T_{1/2} \; / \; T_{1/2}^2)$. Therefore, the relative sensitivity can be defined as,

$$s_{f\lambda} = \left(\frac{\lambda \, t_i \, e^{-\lambda ti}}{1 - e^{-\lambda ti}} - \lambda \, t_w + \frac{\lambda \, t_c \, e^{-\lambda t_c}}{1 - e^{-\lambda t_c}} - 1 \right). \tag{3.42}$$

The final covariance matrix for the measure cross-sections can be calculated utilizing the sandwich formula:

$$(V_\sigma)_{ij} = \sum_r e_{ik} \, S_{ijk} \, e_{jk}, \tag{3.43}$$

where S_{ijk} are the micro-correlation matrices. The correlation matrix can be calculated using (V_σ) and following Eq. (3.42). The uncertainty in cross-section is then determined by calculating the square root of the diagonal elements $((V_\sigma)_{ij}^{1/2})$ of the covariance matrix.

3.5 Measurement of ^{58}Ni(n, p)^{58}Co Reaction Cross-section

Over the years, several reactor-grade steel alloys have utilized nickel (Ni) isotopes [10]. Ni is also utilized in reactor cladding alloys such as Zircaloy-2 [11]. The composition of Ni and Fe in Zircaloy-4 has been controlled to provide a less hydrogen-producing cladding material [11]. Ni is a good candidate to be employed in the ITER and ADSs because of its physical and chemical properties. The high energy neutron interaction leads to different reactions such as (n, γ), (n, p), (n, 2n), (n, α), (n, np), (n, nα), (n, 3n). The cross-section data for some of these reactions are essential for estimating radiation damage to the surrounding structural and reactor cladding materials and for the evaluation of hydrogen production. The (n, p) reaction channel with the ^{58}Ni isotope results in the formation of the medium-lived radioisotope ^{58}Co, which has many medical applications. Its primary function is as a trace element essential for the absorption of vitamin B12 within the human body [12].

This work aims to measure the production cross-section of the ^{58}Co isotope with neutrons generated using the $^{7}\mathrm{Li}(\mathrm{p}, \mathrm{n})$ reaction. The cross-section of the specified reaction was determined relative to the $^{115}\mathrm{In}(\mathrm{n}, \mathrm{n}')^{115\mathrm{m}}\mathrm{In}$ reference monitor reaction cross-section at incident spectrum average neutron energies of 1.66 ± 0.14, 2.06 ± 0.14 and 2.66 ± 0.16 MeV. As the measurements are relative to the reference monitor cross-section and the detector efficiencies, the uncertainty in the measured data is also influenced by the reference monitor cross-sections. The results are reported with a detailed description of uncertainties and the correlation among the measured data using the error propagation method. In this study, a comprehensive covariance analysis was conducted to account for the errors from each attribute and estimate the uncertainty in the measured data. The current findings were evaluated against the available cross-section data in the EXFOR database [13] and the theoretical predictions from the TALYS-1.96 nuclear reaction code [14]. The impacts of different level density models incorporated in the code were also assessed to achieve an improved representation of the existing experimental data. The results were analyzed in comparison with the Evaluated Nuclear Data Library (ENDF/B-VIII.0)[15], Joint Evaluated Fission and Fusion File (JEFF-3.3)[16], Japanese Evaluated Nuclear Data Library (JENDL-4.0)[17], and Chinese Evaluated Nuclear Data Library (CENDL-3.2)[18].

The present study offers a thorough investigation of the significance of error propagation in the neutron-induced nuclear reaction cross-sections data and the TALYS-1.96 nuclear reaction code. The use of the ^{58}Co isotope in medical applications is another area in which the measured data have considerable importance.

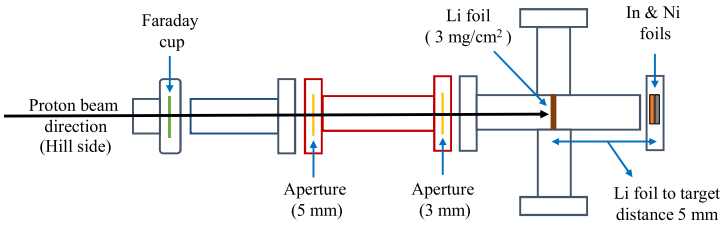

Fig. 3.3: Schematic representation of the experimental setup for the sample irradiation.

3.5.1 Experimental Details

Neutron Production

The present experiment was performed at FOTIA facility at BARC, Mumbai, India. A schematic of the experimental arrangement is shown in Fig. (3.3). In the present experiment, the proton beams of energies 3.6, 4.0 and 4.6 MeV were bombarded on a 3 $\mathrm{mg/cm^2}$ (56.18 μm) thick natural lithium target to produce neutrons through the $^{7}\mathrm{Li(p,n)^{7}Be}$ (Q value = -1.644 MeV; $\mathrm{E_{th}}$ = 1.880 MeV) reaction.

The samples were irradiated with a proton beam current of $\sim$ 25 nA at a distance of 5 mm from the lithium target. The time-of-flight method could not be applied to measure the neutron energy profile as the proton beam was continuous. As a result, the Energy of Proton Energy of Neutron (EPEN)[19] simulation code was employed to generate a neutron energy profile. EPEN is a deterministic simulation code developed to evaluate the neutron energy profile using the $^{7}\mathrm{Li(p,n)^{7}Be}$ reaction. The code operates for incident proton energies ranging from a reaction threshold of 1.880 MeV to a maximum energy of 7.0 MeV. Further information on the specific input parameters and theoretical framework employed by the EPEN code to generate neutron energy distribution can be explored in Reference [19]. The production of a primary group of neutrons $(\mathrm{p,n_0})$ from the ground state of $^{7}\mathrm{Be}$ from the $^{7}\mathrm{Li(p,n)}$ reaction was contaminated by the presence of lower energy secondary neutrons $(\mathrm{p,n_1})$ generated from the $^{7}\mathrm{Li(p,n_1)^{7}Be^{*}}$ ($\mathrm{E_{th}}$ = 2.37 MeV) reaction channel, as well as the neutron yield from the $^{7}\mathrm{Li(p,n+^{3}He)^{4}He}$ ($\mathrm{E_{th}}$ = 3.70 MeV) reaction channel because the current proton energies are above the corresponding reaction threshold. However, in the current proton energy range, the contribution of the $^{7}\mathrm{Li(p,n+^{3}He)^{4}He}$ reaction channel to the neutron yield was negligible. However, the contribution of the $(\mathrm{p,n_0})$ channel to the neutron yield was maximum and was approximately 90%, followed by that of the $(\mathrm{p,n_1})$ channel, which was less than 10% [20, 21]. With the EPEN code, it is possible to acquire the individual $(\mathrm{p,n_0})$ and $(\mathrm{p,n_1})$ neutron energy distribution as well as the total neutron energy distribution from both groups for a specified incident proton energy.

The neutron flux energy spectra for $(\mathrm{p,n_0})$ and $(\mathrm{p,n_1})$ produced from the EPEN code are shown in Fig. (3.4) for all the three energies. A spread in the

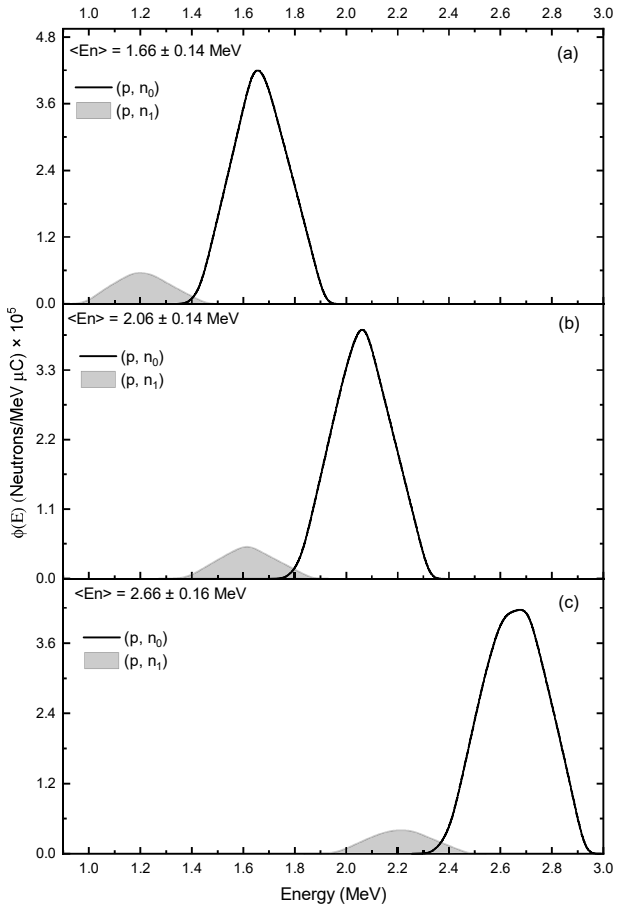

Fig. 3.4: Neutron flux energy spectra $\phi(\mathrm{E})$ produced from the EPEN code for (a) $\mathrm{E_p}$ = 3.60 $\pm$ 0.02 MeV, (b) $\mathrm{E_p}$ = 4.00 $\pm$ 0.02 MeV, and (c) $\mathrm{E_p}$ = 4.60 $\pm$ 0.02 MeV.

neutron spectrum of $(\mathrm{p}, \mathrm{n_0})$ can be observed because of the energy degradation of protons in the ^{7}Li target. The average neutron energy of the $^7\mathrm{Li}(\mathrm{p}, \mathrm{n_0})^7\mathrm{Be}$ neutron group was determined using the equation below [22, 23]:

$$\langle \mathrm{E_n} \rangle = \frac{\int_{\mathrm{E_{min}}}^{\mathrm{E_{max}}} \phi_0(\mathrm{E})\ \mathrm{E}\ \mathrm{dE}}{\int_{\mathrm{E_{min}}}^{\mathrm{E_{max}}} \phi_0(\mathrm{E})\ \mathrm{dE}}, \tag{3.44}$$

where $\phi_0(\mathrm{E})$ is the $(\mathrm{p}, \mathrm{n_0})$ neutron flux energy spectrum from EPEN, and the corresponding integration limits are $\mathrm{E_{min}}$ = 1.313, 1.693, 2.255 and $\mathrm{E_{max}}$ = 1.979, 2.384, 2.989 for incident proton energies of 3.6, 4.0, and 4.6 MeV, respectively. The spectrum averaged neutron energy ($\langle \mathrm{E_n} \rangle$) along with its corresponding uncertainties determined from the EPEN code are 1.66 $\pm$ 0.14, 2.06 $\pm$ 0.14 and 2.66 $\pm$ 0.16 MeV for $\mathrm{E_p}$= 3.6, 4.0, and 4.6 MeV, respectively. The uncertainties were estimated using the neutron energy distribution's full width at half maximum (FWHM).

Table 3.1: Sample details along with their irradiation, cooling, and counting time used in the experiment.

Sample	$\langle E_n \rangle$ (MeV)	Sample weight (mg)	Irradiation time (s)	Cooling time (s)	Counting time (s)
Ni	1.66 ± 0.14	246.7 ± 0.1	86460	102990	64800
	2.06 ± 0.14	308.3 ± 0.1	24180	402340	72000
	2.66± 0.16	276.4 ± 0.1	55020	119420	72000
In	1.66± 0.14	90.8 ± 0.1	86460	5860	900
	2.06± 0.14	93.9 ± 0.1	24180	2040	600
	2.66± 0.16	94.0 ± 0.1	55020	3660	600

Table 3.2: Spectroscopic data used in the present experiment [7].

Reaction	Prominent γ-ray energy (keV)	Branching intensity (%)	Decay mode (%)	Half-life	Spin state J^{π}
^{115}In(n, n′)^{115m}In	336.241 ± 0.025	45.90 ± 0.10	β^{-1} (5) IT (95)	4.486 ± 0.004 h	$1/2^{-1}$
^{58}Ni(n, p)^{58}Co	810.759 ± 0.002	99.45 ± 0.01	ε (100)	70.86 ± 0.06 d	2^{+}

Sample Preparation and γ-ray Spectrometry

In the present experiment, the samples were prepared in three different sets. Natural nickel (Ni) foils having a purity of 99.5 % and thickness of 300 μm were utilized for the experiment. Natural indium (In) foils with 99.97 % purity and thickness of 100 μm were used for monitoring the neutron flux. The Ni and In foils were individually wrapped with 14 μm thick aluminium foil to prevent radioactive cross-contamination among the target, monitor foils, and surroundings. The samples were irradiated by positioning a stack of "Ni – In" with dimensions 1 cm × 1 cm at zero degrees relative to the beam axis. All the foils were accurately weighted using a micro-balance machine to 0.1 mg accuracy. The details regarding the sample's irradiation, cooling, and counting time, as well as weight with the corresponding uncertainty, are listed in Table 3.1.

Upon completion of the irradiation process, the radioactive samples were meticulously removed from the beam line and subsequently allowed to cool for a sufficient period. After sufficient cooling, the irradiated Ni and In samples were affixed to a distinct perspex plate and then transported to the counting room. The Ni-samples were counted for 16 to 18 h and the In-samples were counted for 10 to 15 min to build up sufficient counting statistics according to the induced activity following their half-life. More details regarding irradiation, cooling, and counting times are given in Table 3.1. A pre-calibrated high-purity germanium (HPGe) detector with 50% relative efficiency (manufactured by Baltic Scientific Instruments) was employed for data acquisition. The detector was lead shielded to minimize background interference. The data was acquired utilizing a 16K

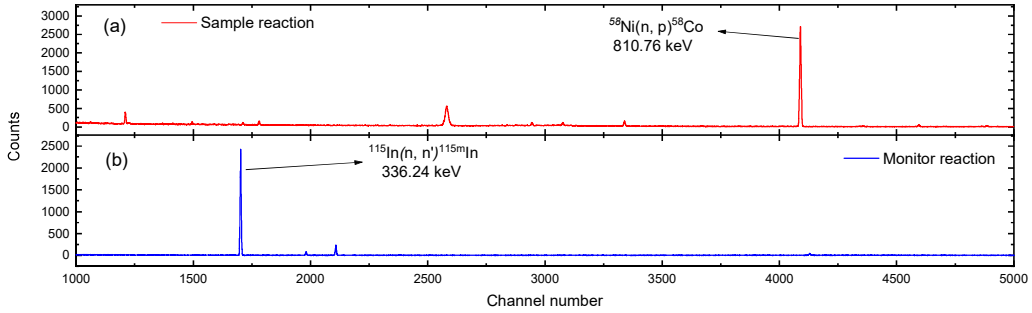

Fig. 3.5: Typical produced γ-ray spectra for (a) ^{58}Ni(n, p)^{58}Co and (b) ^{115}In(n, n′)^{115m}In.

BOSON Multi-Channel Analyzer (MCA) linked with a PC. The dead time of the HPGe detector during the counting was negligible. A schematic drawing of the geometry of the setup for the sample with respect to the HPGe detector is illustrated in Fig. (3.6). The characteristic γ-ray energy and the associated nuclear spectroscopic data for the reaction under study were obtained from the online database NuDat 3.0 [7] and are listed in Table 3.2. Typical γ-ray spectra for the sample and the monitor reaction in the present experiment are shown in Fig. (3.5).

Efficiency Calibration of HPGe Detector

A standard ^{152}Eu ($t_{1/2}$ = 13.517 $\pm$ 0.009 y [7]) point source with a known activity (A_0 = 6614.71 Bq on 1 Oct. 1999) served as the calibration reference for the efficiency of a single crystal p-type HPGe detector across various characteristic γ-ray energies. The following formula was used to determine the efficiency of the point source,

$$\varepsilon_p = K_f \frac{C}{A_0 \, I_\gamma \, e^{-\lambda T} \, \Delta t}. \tag{3.45}$$

The symbol A_0 denotes the activity of the ^{152}Eu point source at the time of its production. The total number of counts recorded for a specific γ-ray energy, along with its absolute intensity (I_γ) over a counting period (Δt = 2000 s), is represented by C. The decay constant is denoted by λ, while the elapsed time between the production and counting dates is referred to as T. The coincidence summing correcting factor is abbreviated as K_f.

To ensure a high count rate, the samples were placed quite close to the detector (6.0 mm) owing to the relatively low count rate from the ^{58}Ni(n, p)^{58}Co reaction. Therefore, the standard efficiency calibration source was also placed at a distance of 6.0 mm from the detector. This, in turn, produced the coincidence summing effect [22]. The Monte Carlo simulation code EFFTRAN [24] was used to compute the correction factor K_f, and corrections to the measured detector efficiency were made. Description of the ^{152}Eu γ-ray source (e.g., material, dimension, and characteristic x-rays and γ-rays) and HPGe detector specifications, including its dimension, crystal material, crystal hole cavity, end cap, window,

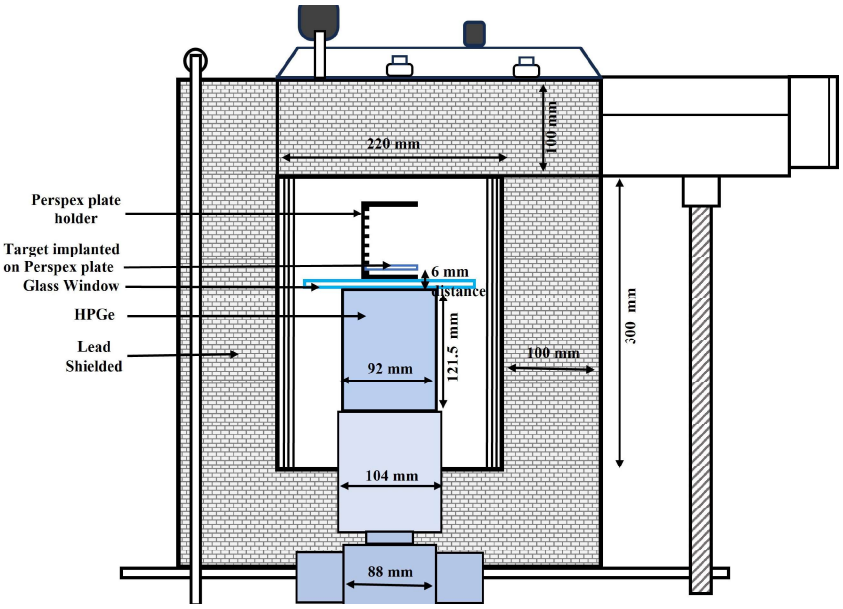

Fig. 3.6: Schematic drawing of the geometry of the setup for the sample w.r.t. the HPGe detector [25].

Table 3.3: Comprehensive data set of the various parameters used in the detector calibration and analysis of the HPGe detector's efficiency measurement.

E_γ (keV)	Counts (C)	I_γ	K_f	ε_p	ε	$\Delta\varepsilon$
121.78	156887	0.2853	1.181	0.0647	0.0564	0.0083
244.70	22998	0.0755	1.227	0.0372	0.0295	0.0078
443.96	6153	0.0283	1.211	0.0263	0.0203	0.0060
964.06	17259	0.1451	1.084	0.0128	0.0097	0.0031
1112.08	15174	0.1367	1.029	0.0114	0.0086	0.0028
1408.01	18509	0.2087	1.052	0.0093	0.0070	0.0023

mount cup, and absorber, are required as inputs for the simulation. The simulation calculates the correction factors for the γ-lines at each of their respective energies while accounting for all possible coincidences between γ-ray and x-ray.

As the activated foil has a finite area ($1\ \mathrm{cm} \times 1\ \mathrm{cm}$) and the HPGe detector's calibration was performed using a point source, the efficiency for the point source geometry ε_p was transferred to the efficiency for the foil geometry ε by EFFTRAN, which is provided in Table 3.3.

3.5.2 Data Analysis

The neutron spectra obtained by the EPEN code were utilized to calculate the neutron flux using the $^{115}\mathrm{In}(\mathrm{n},\mathrm{n}')^{115\mathrm{m}}\mathrm{In}$ reference monitor reaction cross-section. The product $^{115\mathrm{m}}\mathrm{In}$ from this reaction has a prominent γ-line of 336.241 ± 0.025 keV with a half-life ($t_{1/2}$) of 4.486 ± 0.004 h [7]. The flux value was calculated by obtaining the spectral weighted cross-section ($\langle\sigma_m\rangle$) for the monitor reaction,

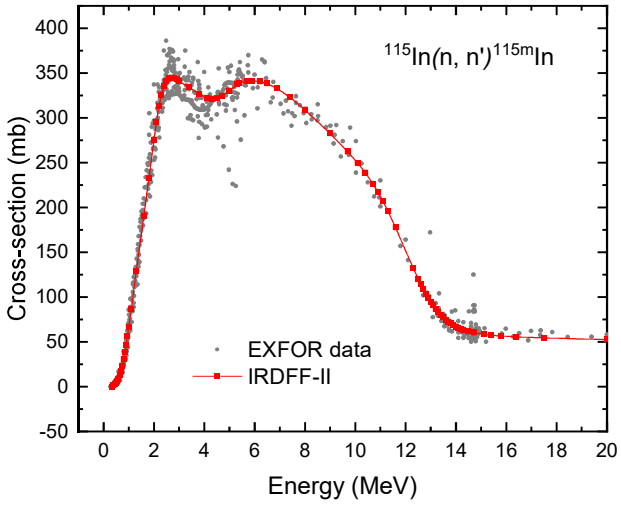

Fig. 3.7: Comparison of $^{115}\mathrm{In}(\mathrm{n},\mathrm{n}')^{115\mathrm{m}}\mathrm{In}$ cross-sections from EXFOR [13] data library and recommended values from the IRDFF-II library[26].

using cross-sections from the IRDFF-II data library and applying Eq. (3.48), as described in the subsequent section. A comparison of the reference monitor cross-sections from the EXFOR [13] data library and recommended values from the IRDFF-II [26] is shown in Fig. (3.7). The net neutron flux incident on the target was calculated using spectral weighted cross-sections at various energies using the Eq. (3.19) [27, 28]. This calculated neutron flux has been used in Eq. (3.20) for the determination of neutron spectrum averaged cross-section.

Due to the presence of quasi-monoenergetic neutrons, the effect of the lower energy tail part can also be observed in the measured cross-sections. As a result, removing the contribution of these neutrons from the measured cross-section is necessary. The correction factor for low-energy background neutrons, along with the self-attenuation factor for γ-ray, is discussed in following subsections.

Correction Factor for Low-energy Background Neutrons

As the present proton energies are above the reaction threshold of the first excited state of $^{7}\mathrm{Be}$, the neutrons produced from the $^{7}\mathrm{Li}(\mathrm{p},\mathrm{n})$ reaction were contaminated by secondary group of lower energy neutrons $(\mathrm{p},\mathrm{n}_1)$ produced from the reaction $^{7}\mathrm{Li}(\mathrm{p},\mathrm{n}_1)^{7}\mathrm{Be}^{*}$ ($\mathrm{E_{th}} = 2.37$ MeV). The precise measurement of neutron induced reaction cross-section requires the subtraction of this $(\mathrm{p},\mathrm{n}_1)$ low-energy background neutron contribution. This has been considered and calculated using Eq. (13) of Reference [22]:

$$\mathrm{N_{corr}} = 1 - \frac{\int_{\mathrm{E_{low}}}^{\mathrm{E_{high}}} \phi_1(\mathrm{E})\ (\sigma_{\mathrm{x}}(\mathrm{E}))\ \mathrm{dE}}{\int_{\mathrm{E_{low}}}^{\mathrm{E_{high}}} \phi(\mathrm{E})\ (\sigma_{\mathrm{x}}(\mathrm{E}))\ \mathrm{dE}}, \tag{3.46}$$

where $\phi_1(\mathrm{E})$ is the $(\mathrm{p},\mathrm{n}_1)$ neutron flux energy spectrum, and $\phi(\mathrm{E}) = \phi_0(\mathrm{E}) + \phi_1(\mathrm{E})$ is the total neutron flux obtained from the EPEN code. The integration

Table 3.4: Correction factors (N_{corr} and G_{self}) applied to the measured cross-sections.

Reaction	$\langle E_n \rangle$ (MeV)	N_{corr}	Sample	E_γ (keV)	G_{self}
^{58}Ni(n, p)^{58}Co	1.66 ± 0.14	0.9708	Ni	810.759 ± 0.002	1.0092
	2.06 ± 0.14	0.9590			
	2.66 ± 0.16	0.9600			
$^{115}\mathrm{In}(\mathrm{n}, \mathrm{n}')^{115\mathrm{m}}\mathrm{In}$	1.66 ± 0.14	0.9339	In	336.241 ± 0.025	1.0051
	2.06 ± 0.14	0.9236			
	2.66 ± 0.16	0.9250			

limit for incident proton energies of 3.6, 4.0, and 4.6 MeV corresponding to $(\mathrm{p}, \mathrm{n}_1)$ neutron spectra are E_{low}= 0.884, 1.27, 1.836 and E_{high}= 1.521, 1.931, 2.542, respectively. For the total neutron flux, these limits are E_{low}= 0.884, 1.27, 1.836 and E_{high}= 1.979, 2.384, 2.989. $\sigma_x(E)$ is the ^{58}Ni(n, p)^{58}Co reaction cross-section taken from the ENDF/B-VIII.0 [15] and the $^{115}\mathrm{In}(\mathrm{n}, \mathrm{n}')^{115\mathrm{m}}\mathrm{In}$ reaction cross-section taken from the IRDFF-II library [26]. The correction factors for the three neutron energies are presented in Table 3.4.

Self-attenuation Factor for γ-ray

The current study addressed the correction factor for the self-attenuation of γ-rays resulting from their interaction with the samples. The correction factor was calculated using Eq. (3.47), which considers the γ-ray flux passing through a sample of thickness t and density ρ, along with the mass attenuation coefficient μ_m.

$$G_{self} = \frac{\mu_m \, \rho \, t}{1 - \exp(-\mu_m \, \rho \, t)}, \tag{3.47}$$

where μ_m is determined using data from XMuDat 1.0.1 [29]. The calculated correction factor for γ-ray self-attenuation for nickel and indium samples is provided in Table 3.4.

Cross-sections for Reference Monitor Reactions and their Correlation Matrix

The standard data library for neutron monitor reaction cross-section IRDFF-II [26] was used for reference monitor reaction cross-section $^{115}\mathrm{In}(\mathrm{n}, \mathrm{n}')^{115\mathrm{m}}\mathrm{In}$. As the neutrons generated by the $^{7}\mathrm{Li}(\mathrm{p}, \mathrm{n}_0)^{7}\mathrm{Be}$ reaction are not monoenergetic but rather have an energy spread, the neutron flux energy spectrum $\phi_0(E)$ produced by the EPEN [19] code was used to fold the point-wise monitor cross-section in the IRDFF-II library ($\sigma_m(E)$) using the following equation [22]:

$$\langle \sigma_m \rangle = \frac{\int_{E_{min}}^{E_{max}} \phi_0(E) \, \sigma_m(E) \, dE}{\int_{E_{min}}^{E_{max}} \phi_0(E) \, dE}. \tag{3.48}$$

The energy integrated neutron flux calculated from the γ-ray activity of

^{115m}In after substantiating the contribution of low-energy background neutrons with γ-ray self attenuation correction is 1.222×10^7 n cm^{-2} s^{-1} at 2.66 MeV, 1.548×10^7 n cm^{-2} s^{-1} at 2.06 MeV, and 2.415×10^7 n cm^{-2} s^{-1} at 1.66 MeV neutron energy. The covariance information of $\sigma_m(E)$ is provided by the IRDFF-II for its group-wise cross-section. Similar to this, we have also introduced the group-wise neutron flux energy spectrum $\phi_{i,k}$, produced using the EPEN code by

$$\phi_{i,k} = \int_{E_{k,low}}^{E_{k,high}} \phi_i(E)\, dE, \tag{3.49}$$

which fulfills $\sum_k \phi_{i,k} = 1$, where i = 1, 2, and 3 are specified for $\langle E_n \rangle$ = 1.66, 2.06 and 2.66 MeV, respectively. The energy group boundaries in the IRDFF-II library have k energy groups defined for each neutron energy i. The lower and upper boundaries of the k^{th} energy group are denoted by $E_{k,low}$ and $E_{k,high}$ respectively. Table 3.5 lists the group-wise quantities for the spectrum averaged neutron energy flux, IRDFF-II monitor cross-sections, and its uncertainty and correlation coefficients, where groups k = 1-3, 4-6, 7-9 are specified for $\langle E_n \rangle$ = 1.66, 2.06, and 2.66 MeV neutrons, respectively.

Reference [9] was used for propagating the covariance matrix of the IRDFF-II library to the averaged cross-section with the following equation:

$$Cov(\langle \sigma_m \rangle_i, \langle \sigma_m \rangle_j) = \sum_{k=1}^{N} \sum_{l=1}^{N} \phi_{i,k}\, Cov(\sigma_k, \sigma_l)\, \phi_{j,l}, \tag{3.50}$$

where N denotes the number of points in the specified group, and

$$Cov(\sigma_k, \sigma_l) = Cor(\sigma_k, \sigma_l)\, \Delta\sigma_k\, \Delta\sigma_l. \tag{3.51}$$

The correlation coefficients were propagated between the averaged cross-sections using the generated covariance matrix, as follows:

$$Cor(\langle \sigma_m \rangle_i, \langle \sigma_m \rangle_j) = \frac{Cov(\langle \sigma_m \rangle_i, \langle \sigma_m \rangle_j)}{\Delta\langle \sigma_m \rangle_i\, \Delta\langle \sigma_m \rangle_j}. \tag{3.52}$$

The neutron spectrum averaged monitor cross-section $\langle \sigma_m \rangle$ for each energy is presented in Table 3.6, along with its uncertainty and correlation coefficients.

3.5.3 Results and Discussion

The reaction cross-sections for the ^{58}Ni(n, p)^{58}Co reaction were measured using quasi-monoenergetic neutrons produced from the ^{7}Li(p, n) reaction at neutron spectrum average energies of 1.66 $\pm$ 0.14, 2.06 $\pm$ 0.14 and 2.66 $\pm$ 0.16 MeV. The present measurements were performed using the offline γ-ray spectrometric technique followed by neutron activation analysis. The neutron flux was cal-

Table 3.5: IRDFF-II [26] spectrum averaged neutron monitor cross-sections (σ_k) along with fractional uncertainties and correlation coefficients and EPEN code computed fractional neutron flux for each neutron energy group.

i	k	$E_{k,low}$ (MeV)	$E_{k,high}$ (MeV)	$\phi_{i,k}/\sum\phi_{i,k}$	σ_k (b)	$\Delta\sigma_k$ (%)	Correlation coefficient $Cor(\sigma_k, \sigma_l)$ 1.313	1.600	1.800	1.600	2.000	2.200	2.400	2.600	2.800
1	1	1.313	1.600	0.147	0.16130	2.96	1.0000								
	2	1.600	1.800	0.779	0.21193	2.83	0.8434	1.0000							
	3	1.800	2.000	0.074	0.25421	2.68	0.5449	0.8680	1.0000						
2	4	1.600	2.000	0.146	0.24285	2.72	0.8434	1.0000	0.8680	1.0000					
	5	2.000	2.200	0.770	0.29540	2.63	0.2681	0.5180	0.8334	0.5180	1.0000				
	6	2.200	2.400	0.085	0.32591	2.62	0.1734	0.2187	0.4937	0.2187	0.8559	1.0000			
3	7	2.400	2.600	0.154	0.33654	2.61	0.2576	0.1747	0.2708	0.1747	0.5690	0.8707	1.0000		
	8	2.600	2.800	0.720	0.34484	2.57	0.3677	0.2983	0.2361	0.2983	0.3173	0.5712	0.8720	1.0000	
	9	2.800	2.989	0.126	0.34368	2.46	0.4031	0.4162	0.3149	0.4162	0.2253	0.3222	0.6181	0.9021	1.0000

Table 3.6: Neutron spectrum averaged monitor cross-section along with its uncertainty and correlation coefficients.

Reaction	$\langle E_n \rangle$ (MeV)	Cross-section $\langle \sigma_m \rangle$ (mb)	$\Delta\langle \sigma_m \rangle$ (%)	$Cor(\langle \sigma_m \rangle_i, \langle \sigma_m \rangle_j)$		
$^{115}In(n,n')^{115m}In$	1.66 ± 0.14	204.62 ± 5.79	2.83	1.0000		
	2.06 ± 0.14	286.50 ± 7.54	2.63	0.5530	1.0000	
	2.66 ± 0.16	343.00 ± 8.82	2.57	0.2996	0.2993	1.0000

culated using the reference monitor reaction cross-section for $^{115}In(n,n')^{115m}In$ from IRDFF-II. The reported cross-sections are important for estimating the radiation damage to surrounding structural and cladding materials and for the evaluation of hydrogen production. The uncertainties from various attributes were propagated into the measured cross-sections using the ratio method of covariance technique. The overall uncertainty in the measured cross-section data was found to be less than 6 %. The present measured reaction cross-sections with their uncertainties calculated using the covariance analysis are presented in Table 3.6. The obtained results were compared with the existing experimental data and with the theoretical results using the nuclear reaction code TALYS, as depicted in Fig. (3.8) . The results of the evaluated data libraries, like ENDF/B-VIII.0, JEFF-3.3, JENDL-4.0, and CENDL-3.2, were also compared with the present measured data along with the literature data, as shown in Fig. (3.9). In general, the measured data were found in good agreement with the evaluated data, theoretical model predictions, and existing data in literature.

The experimentally measured ^{58}Ni(n, p)^{58}Co reaction cross-sections were also compared with the theoretical values obtained using the SDM as shown in Fig. (3.10). The SDM predictions are in consensus with the experimental data except for the low-energy region, where the cross-section is underestimated because the collective excitations are naturally incorporated by the configuration mixing through the residual interaction. For the NLDs from different models as available in the TALYS, the collective effects are included through the vibrational and rotational enhancement factors, and their NLDs are further normalized at low energies with neutron resonance data [30].

Comparison of Experimental Methodology with Earlier Measurements: Improvements in the Current Study

The comparison of experimental conditions and different corrections for some recent ^{58}Ni(n, p)^{58}Co reaction cross-section is summarized in Table 3.7. A majority of the recent measurements are reported without a detailed covariance analysis. The importance of generating covariance data for assessing uncertainties in nuclear power safety has been highlighted by the nuclear data community. However, many older experiments do not contain the data needed to produce covariance. Therefore, the present measurements are reported with detailed uncertainty analysis utilizing the covariance technique. The obtained cross-sections are also corrected for coincidence summing, low energy background neutrons,

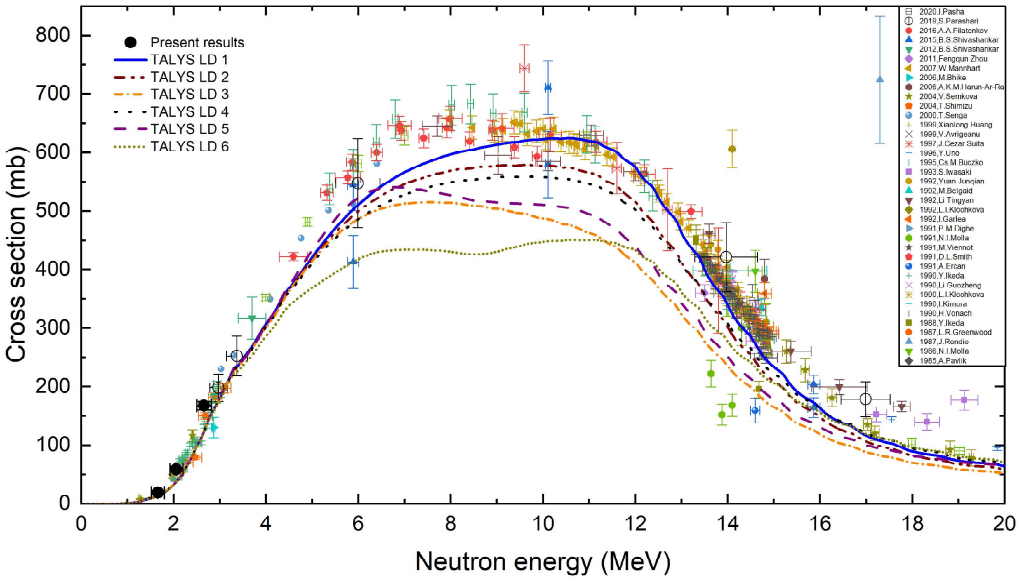

Fig. 3.8: Experimentally measured ^{58}Ni(n, p)^{58}Co reaction cross-sections compared with the existing literature data and various level density models available in the TALYS code [14].

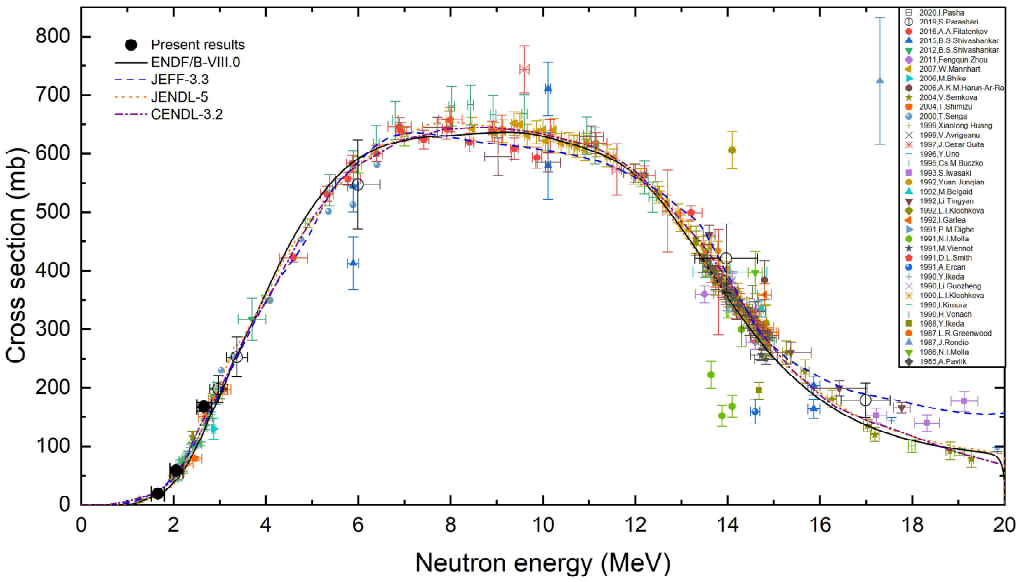

Fig. 3.9: Experimentally measured ^{58}Ni(n, p)^{58}Co reaction cross-sections compared with the existing literature data and various evaluated data libraries such as ENDF/B-VIII.0 [15], JEFF-3.3 [16], JENDL-5.0 [17], and CENDL-3.2 [18].

Table 3.7: Comparison of experimental conditions and different corrections for some of the recent $^{58}\mathrm{Ni}(\mathrm{n},\mathrm{p})^{58}\mathrm{Co}$ reaction cross-section [13].

Author (Year)	Neutron source	Flux monitor reaction	Threshold energy (MeV)	Neutron energy (MeV)	Covariance	Corrections			Reference
						Coincidence summing	Low-energy background neutrons	Self-attenuation for γ-rays	
Hingu et al. (2023)	$^{7}\mathrm{Li}(\mathrm{p},\mathrm{n})$	$^{115}\mathrm{In}(\mathrm{n},\mathrm{n}')^{115\mathrm{m}}\mathrm{In}$	0	1.66, 2.06 and 2.66	yes	yes	yes	yes	Present work
Pasha et al. (2020)	$^{3}\mathrm{H}(\mathrm{d},\mathrm{n})^{4}\mathrm{He}$	$^{197}\mathrm{Au}(\mathrm{n},2\mathrm{n})^{196}\mathrm{Au}$	0	14.54	yes	yes	yes	yes	[37]
Parashari et al. (2019)	$^{7}\mathrm{Li}(\mathrm{p},\mathrm{n})$	$^{115}\mathrm{In}(\mathrm{n},\mathrm{n}')^{115\mathrm{m}}\mathrm{In}$	0	5.99, 13.97 and 16.99	yes	yes	yes	no	[38]
		$^{197}\mathrm{Au}(\mathrm{n},\gamma)^{198}\mathrm{Au}$	0	2.97 and 3.37	yes	yes	yes	no	
Filatenkov et al. (2016)	$^{3}\mathrm{H}(\mathrm{d},\mathrm{n})^{4}\mathrm{He}$	$^{93}\mathrm{Nb}(\mathrm{n},2\mathrm{n})^{92\mathrm{m}}\mathrm{Nb}$	8.93	13.47 – 14.86	no	yes	yes	yes	[39]
Shivashankar et al. (2015)	$^{7}\mathrm{Li}(\mathrm{p},\mathrm{n})$	$^{232}\mathrm{Th}(\mathrm{n},\mathrm{f})^{97}\mathrm{Zr}$ and $^{238}\mathrm{U}(\mathrm{n},\mathrm{f})^{97}\mathrm{Zr}$	0	5.89, 10.11, and 15.87	yes	no	yes	no	[8]
Shivashankar et al. (2012)	$^{7}\mathrm{Li}(\mathrm{p},\mathrm{n})$	$^{115}\mathrm{In}(\mathrm{n},\mathrm{n}')^{115\mathrm{m}}\mathrm{In}$	0	3.7	no	no	no	no	[40]
Zhou et al. (2011)	$^{3}\mathrm{H}(\mathrm{d},\mathrm{n})^{4}\mathrm{He}$	$^{27}\mathrm{Al}(\mathrm{n},\alpha)^{24}\mathrm{Na}$	3.25	around 14	no	yes	no	yes	[41]
Mannhart et al. (2007)	D-D fusion	$^{27}\mathrm{Al}(\mathrm{n},\alpha)^{24}\mathrm{Na}$ and $^{238}\mathrm{U}(\mathrm{n},\mathrm{f})^{97}\mathrm{Zr}$	3.25 and 0	7.98 – 14.42	yes	no	yes	yes	[42]
Harun-Ar-Rashid et al. (2006)	$^{3}\mathrm{H}(\mathrm{d},\mathrm{n})^{4}\mathrm{He}$	$^{27}\mathrm{Al}(\mathrm{n},\alpha)^{24}\mathrm{Na}$	3.25	14.8	no	no	no	no	[43]
Bhike et al. (2006)	$^{7}\mathrm{Li}(\mathrm{p},\mathrm{n})$	$^{197}\mathrm{Au}(\mathrm{n},\gamma)^{198}\mathrm{Au}$	0	2.87	no	no	no	no	[44]
Semkova et al. (2004)	$^{3}\mathrm{H}(\mathrm{d},\mathrm{n})^{4}\mathrm{He}$	$^{27}\mathrm{Al}(\mathrm{n},\alpha)^{24}\mathrm{Na}$	3.25	1.29 – 20.34	no	yes	yes	yes	[10]
Shimizu et al. (2004)	D-D fusion	$^{115}\mathrm{In}(\mathrm{n},\mathrm{n}')^{115\mathrm{m}}\mathrm{In}$	0	2.09 – 3.09	no	yes	yes	yes	[45]
Senga et al. (2000)	D-D fusion	$^{115}\mathrm{In}(\mathrm{n},\mathrm{n}')^{115\mathrm{m}}\mathrm{In}$	0	1.99 – 6.41	no	no	no	no	[46]

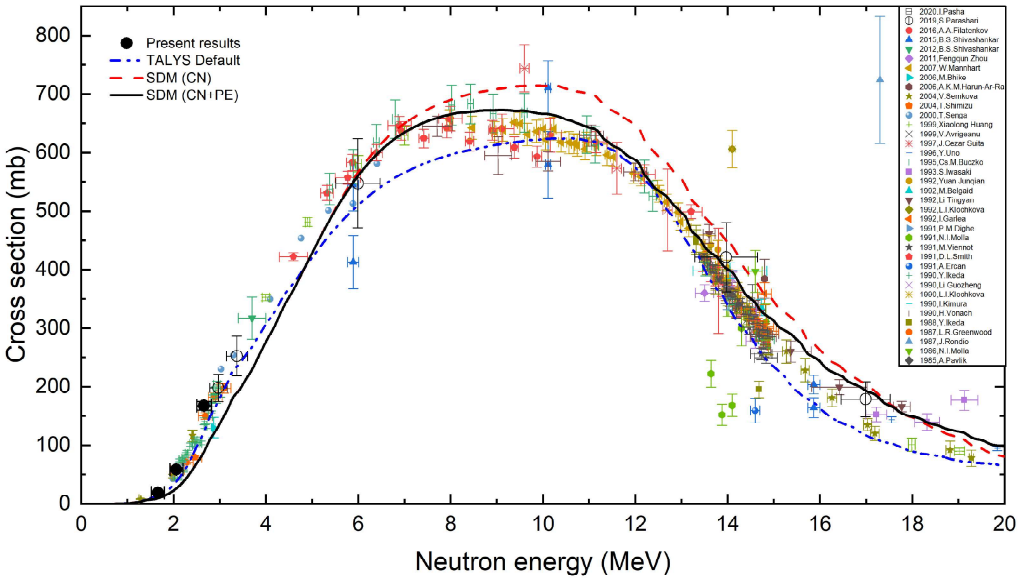

Fig. 3.10: Experimentally measured ^{58}Ni (n, p)^{58}Co reaction cross-sections compared with the existing literature data, TALYS default calculations, and NLDs obtained using the SDM [30–36].

and self attenuation for γ-rays.

3.5.4 Summary and Conclusions

The neutron activation analysis, coupled with an offline γ-ray spectrometric method, was applied to measure the production cross-section of ^{58}Co using quasi-monoenergetic neutrons from the $^{7}\mathrm{Li(p,n)}$ reaction. The measured cross-sections were normalized against the reference cross-section of the $^{115}\mathrm{In(n,n')}^{115\mathrm{m}}$In reaction as provided by IRDFF-II. The uncertainties and correlations among the measured cross-sections were calculated in detail using covariance analysis. The measured data were generally observed to be consistent with the literature data, evaluated data libraries such as ENDF/B-VIII.0, JEFF-3.3, JENDL-4.0 and CENDL-3.2, and theoretical computations performed with the nuclear reaction code TALYS. To provide a more accurate representation of the measured results, the effects of various level density models within the TALYS code was assessed. It is recommended to use the error propagation method to determine the correlations between the monitor reaction cross-sections because these cross-sections can lead to significant uncertainty in the measured data. Accurate determination of reaction cross-sections and their associated uncertainties provides critical insights for optimizing the safety and efficiency of nuclear technologies. Furthermore, the current work is vital for advancing medical accelerator technologies and for accurate dose calculation of the medical isotope ^{58}Co, which is produced via the ^{58}Ni(n, p)^{58}Co reaction. As a critical isotope for cancer radiotherapy, comprehensive knowledge of its reaction cross-section and associated uncertainties is vital for refining production techniques, securing a consistent supply of

medical isotopes, and maintaining rigorous quality control in isotope production facilities.

3.6 Measurement of ^{115m}In Production Cross-section

Indium (In) occurs naturally with two stable isotopes, $^{113}\mathrm{In}$ and $^{115}\mathrm{In}$, with relative abundances of 4.29 % and 95.71 %, respectively. In is used in an alloy that is popular for making control rods in the nuclear reactor. The control rod is a key component of a reactor which controls the fission rate of the fuel to sustain the optimal operation of the reactor. Therefore the knowledge of the composition material of the control rod and the interaction probability of neutron is quite important [47]. In is also extensively employed for determining neutron flux, which is necessary for calculating neutron-induced reaction cross-sections.

Accurate neutron flux measurement is crucial to estimate the experimental reaction cross sections. The incident neutron flux on the target sample must be measured using an appropriate flux monitor. There are certain conditions for reactions to act as flux monitor reactions which is discussed in our earlier publication [48]. Additionally, the reaction employed as a flux monitor must have a suitable threshold corresponding to the reaction being measured. For example if we use $^{27}\mathrm{Al}(\mathrm{n},\alpha)$ reaction as flux monitor which has threshold around 3.4 MeV, for the reaction which has no threshold then the flux calculated with Al will only give information of neutron flux above 3.4 MeV not below that. So we will get less value of neutron flux and corresponding higher value of cross section. So the flux monitor reaction must have less value of threshold in comparison with the reaction being measured for accurate determination of neutron flux.

The aim of this study is to determine cross-sections for the production of $^{115m}\mathrm{In}$ by quasi-monoenergetic neutrons. In the current work, we have measured the cross-section data for $^{115}\mathrm{In}(\mathrm{n},\mathrm{n}')^{115m}\mathrm{In}$ nuclear reaction for the incident neutron energies of $7.89 \pm 0.66, 12.95 \pm 0.70, 15.97 \pm 0.75, 16.99 \pm 0.75, 18.99 \pm 0.83$ MeV. The cross-section of the aforesaid reaction was also compared to literature data taken from EXFOR [49] and with the results of theoretical model codes, TALYS-1.95 [50] and EMPIRE-3.2.3 [51]. The impact of various level density models from both codes was assessed to enhance the representation of current and literature data. The measured data are also compared with different evaluated data libraries such as ENDF/B-VIII.0 [15], JEFF-3.3 [16], JENDL-4.0 [17], CENDL-3.2 [18]. Since the current study relies on relative measurements, covariance analysis [8, 9] is employed to assess the uncertainties in the measured cross-sections. The uncertainty and relative correlation among the many parameters, employed in this measurement, were determined by using covariance analysis.

3.6.1 Experimental Details

Neutron Production

The measurement of the reaction cross-section for the $^{115}\mathrm{In}(\mathrm{n},\mathrm{n}')^{115\mathrm{m}}\mathrm{In}$ reaction at five different neutron energies was conducted at the 14UD Pelletron accelerator facility within BARC-TIFR in Mumbai, India, utilizing the standard activation technique and subsequent offline γ-ray spectroscopy. Quasi-monoenergetic neutrons were produced via the $^{7}\mathrm{Li}(\mathrm{p},\mathrm{n})$ reaction with proton beams of 10, 15, 18, 19, and 21 MeV energies. These proton beams were directed at a natural lithium (Li) target with a thickness of $8\ \mathrm{mg/cm^2}$. The Li foil was prepared on the day of the experiment and promptly positioned within the target assembly in the target laboratory. To ensure that the sample is exclusively exposed to the produced neutrons and to terminate the proton beam, the Li foil was encased in tantalum (Ta) foil. This Ta foil plays a crucial role in the generation of neutrons. A (Ta) foil, with a thickness of $\approx 4\ \mathrm{mg/cm^2}$, was positioned in front of the lithium (Li) target facing the proton beam. Meanwhile, a thicker Ta foil, measuring 0.1 mm in thickness, was placed behind the lithium target to effectively stop the proton beam. This completely shields the In target from proton exposure. The SRIM code was employed to determine the degradation of both protons and neutrons at each stage of the $\mathrm{Ta-Li-Ta}$ stack [52]. A schematic representation of the experimental setup is presented in Fig. (3.11).

Neutrons were generated through the interaction of the proton beam with the natural Li foil. As a result of this interaction, a range of reactions occur. The formation of the $^{7}\mathrm{Be}$ ground state from the $^{7}\mathrm{Li}(\mathrm{p},\mathrm{n})$ reaction is the primary outcome, with a threshold energy of 1.88 MeV, while the threshold energy for its first excited state is 2.38 MeV. This reaction results in the primary peak, as illustrated in Fig. (3.12). The population of the first excited state of $^{7}\mathrm{Be}$ generates a secondary neutron group at a proton energy exceeding 2.38 MeV. Consequently, two neutron groups, $\mathrm{n_0}$ and $\mathrm{n_1}$, account for the neutron distribution, arising from the population of both the ground state and the first excited state of $^{7}\mathrm{Be}$. In addition to the primary neutron group, the three-body interaction and other excited states contribute to the neutron generation above 6 MeV [28], as a result, a continuous neutron energy distribution is produced. The continuous neutron spectrum was generated using the neutron energy distribution reported in References [53, 54]. These neutron spectra contain a quasi-monoenergetic peak at $\mathrm{E_p - 1.88\ MeV}$ and a long continuum towards lower energy, as seen in Fig. (3.12), due to contributions from various reaction channels. The tail region is a continuum consisting of neutrons with lower energies that affect the reaction cross-section. As a result, the influence from the tail end of the neutron spectrum must be eliminated. This can be done by taking into account spectral average cross-sections [55], as discussed in the subsequent section.

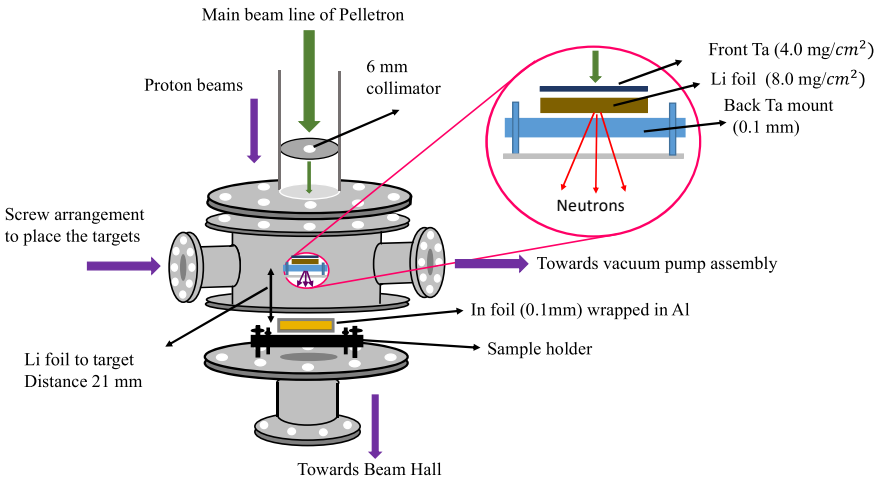

Fig. 3.11: Schematic representation of the experimental setup [28, 38] utilized for sample irradiation.

Table 3.8: Details regarding the irradiation employed in the current experiment.

	Irradiation 1	Irradiation 2	Irradiation 3	Irradiation 4	Irradiation 5
Proton energy (MeV)	21	18	15	10	19
Neutron energy (MeV)	18.99 ± 0.83	15.97 ± 0.75	12.95 ± 0.70	7.89 ± 0.66	16.92 ± 0.75
Irradiation time (h : min)	7:00	7:00	9:05	8:15	2:58
Cooling time (h : min)	0:58	1:28	0:56	1:03	0:48
Beam current (nA)	150	150	150	120	150
Indium weight (g)	0.0756	0.0756	0.0771	0.0666	0.0816

Sample Preparation and γ-ray Spectrometry

The natural In foils, with a purity of 99.97% and an area of 1 cm× 1 cm, were employed in the study. The weights of the In samples for different proton energies were 0.0756 g (21 MeV), 0.0816 g (19 MeV), 0.0756 g (18 MeV), 0.0771 g (15 MeV), and 0.0666 g (10 MeV). These samples were individually covered by thin Al foil to avoid the contamination of radiation from the target to the surrounding. The irradiation of each sample was performed for different irradiation time. The irradiation details are given in Table 3.8. Following irradiation, the sample was given ample time to cool and was thereafter positioned on a perspex plate for γ-ray spectrometry. HPGe detector calibrated with standard ^{152}Eu multi-gamma source and linked with PC-based 4K multichannel analyzer (MCA), was used for the counting of the sample. The data acquisition and analysis were conducted with the CAMAC-based Linux Advanced Multiparameter System (LAMPS) software [56].

Table 3.9: Nuclear spectroscopic data utilized in the present experiment [7].

Reaction	Prominent γ-ray Energy (keV)	Branching Intensity (%)	Decay Mode (%)	Half-Life	Spin State J^{π}
$^{115}\mathrm{In}(\mathrm{n},\mathrm{n}')^{115\mathrm{m}}\mathrm{In}$	336.241 ± 0.025	45.90 ± 0.1	β^{-1} (5) IT (95)	4.486 ± 0.004 h	$1/2^{-1}$
$^{113}\mathrm{In}(\mathrm{n},\mathrm{n}')^{113\mathrm{m}}\mathrm{In}$	391.698 ± 0.003	64.94 ± 0.17	IT (100)	99.476 ± 0.023 min	$1/2^{-1}$

3.6.2 Data Analysis

Neutron spectra obtained by applying the methodology described previously were utilized for the calculation of neutron flux. In the current measurement, $^{113}\mathrm{In}(\mathrm{n},\mathrm{n}')^{113\mathrm{m}}\mathrm{In}$ reaction has been used as a flux monitor. The product $^{113\mathrm{m}}\mathrm{In}$ from this reaction has a prominent γ line of 391.698 ± 0.003 keV which has a half-life $(\mathrm{t}_{1/2})$ of 99.476 ± 0.023 m [7]. To obtain the flux value, a spectral weighted cross-section (σ_{w}) was first calculated for the monitor reaction using the cross-sections taken from the EXFOR data library [49], through the following expression.

$$\sigma_{\mathrm{w}} = \frac{\sum\limits_{\mathrm{E_i}} \phi_{\mathrm{i}}\, \sigma_{\mathrm{i}}}{\sum\limits_{\mathrm{E_i}} \phi_{\mathrm{i}}}, \tag{3.53}$$

where ϕ_{i} and σ_{i} are the neutron flux and corresponding monitor cross-section respectively. At various energies, the net neutron flux ϕ incident on the target has been calculated by using spectral weighted cross-section into the equation (3.19).

This calculated flux has been used in equation (3.20) for determining the reaction cross-section (σ) for the reaction. Here, the peak area of the gamma spectrum was determined using LAMPS software. Using the mass of each target isotope, the number of target nuclei (N_0) was determined. Other standard parameters of the reaction are extracted from the NuDat library [7].

Since we have quasi-monoenergetic neutrons, the contribution of the lower energy tail part also comes in the measured cross-sections. Therefore, a contribution of these neutrons in the measured cross-section must be removed. The correction was done as suggested in the literature [55, 58] by taking spectral average reaction cross-section for neutrons from lowest energy to peak starting neutron energy. This cross-section has been subtracted from the measured cross-section, giving the final cross-section at the spectrum average neutron peak energy.

3.6.3 Results and Discussion

The cross-sections for the $^{115}\mathrm{In}(\mathrm{n},\mathrm{n}')^{115\mathrm{m}}\mathrm{In}$ reaction have been measured at the average neutron energies of $7.89 \pm 0.66, 12.95 \pm 0.70, 15.97 \pm 0.75, 16.99 \pm$

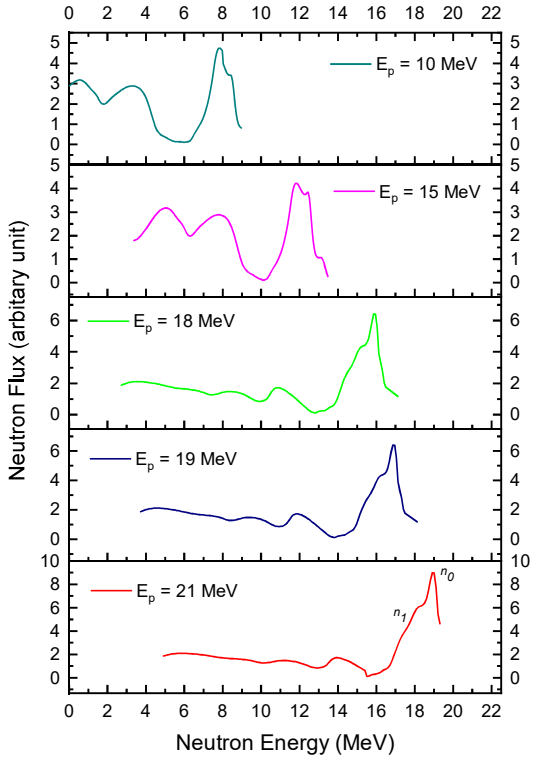

Fig. 3.12: Neutron spectra generated by the $^{7}\mathrm{Li(p,n)}$ reaction with the five distinct energies employed for the irradiations [57].

$0.75, 18.99 \pm 0.83$ MeV by using the NAA technique, relative to $^{113}\mathrm{In(n,n')}^{113m}\mathrm{In}$ monitor reaction. These cross-sections are important in determining the neutron flux, in reactor design as well as improving the nuclear database. The covariance method was used to estimate the uncertainties in the current measurement. The measured cross-sections are shown in the Table 3.10 and also shown in Fig. (3.13). All possible fractional uncertainties associated with various parameters in the measurement of the $^{115}\mathrm{In(n,n')}^{115m}\mathrm{In}$ reaction cross-section were propagated to calculate the total uncertainty in the cross-section. The final correlation matrix for the measured reaction cross-section is presented in Table 3.11. The present results have been compared with the literature data from EXFOR [49] and also with the results of theoretical codes TALYS-1.95 [50] and EMPIRE-3.2.3 [51]. The theoretical cross-section for the selected nuclear reaction was calculated employing various LD models of TALYS 1.95, from LD model 1 to LD model 6, and then compared to experimental data, as illustrated in Fig. (3.13). The LD model 2 of TALYS effectively accounts for the current experimental results within the uncertainty of the measured cross-sections, while other models tend to underestimate the observed data. However, the present data at 18.99 ± 0.83 MeV is lower than the literature data. Different level density options are also available in EMPIRE 3.2.3. The level density parameter values LD = 0, 1, 2, 3, 4

Table 3.10: Comparison of experimentally determined cross-section of $^{115}\mathrm{In}(\mathrm{n},\mathrm{n}')^{115\mathrm{m}}\mathrm{In}$ reaction with the best fit ldmodel (LD-2) of TALYS [14].

Neutron Energy (MeV)	$^{115}\mathrm{In}(\mathrm{n},\mathrm{n}')^{115\mathrm{m}}\mathrm{In}$ reaction cross-section (mb)	
	Experimental	TALYS LD-2
18.99 ± 0.83	36.60 ± 5.29	41.15
15.97 ± 0.75	57.74 ± 6.39	51.33
12.95 ± 0.70	85.99 ± 11.53	83.06
7.89 ± 0.66	331.65 ± 45.27	285.21
16.92 ± 0.75	52.31 ± 7.93	47.41

Table 3.11: Correlation matrix for the measured reaction cross-sections.

Neutron Energy (MeV)	Correlation Matrix				
18.99 ± 0.83	1				
15.97 ± 0.75	0.272	1			
12.95 ± 0.70	0.225	0.293	1		
7.89 ± 0.66	0.221	0.288	0.238	1	
16.92 ± 0.75	0.199	0.260	0.214	0.211	1

are based on several well-known models whose details are available in EMPIRE 3.2.3 manual. The results from different LD models of EMPIRE are overestimated as compared with the present experimental results and also do not agree with the literature data at higher energies. Our results have been compared against various evaluated data libraries, including ENDF/B-VIII.0, JEFF-3.3, JENDL-4.0, CENDL-3.2, as well as literature data, as illustrated in Fig. (3.14).

Improvements in the Current Research When Comparing Experimental Approach to Earlier Measurements

The Experimental conditions in the current as well as prior measurements for $^{115}\mathrm{In}(\mathrm{n},\mathrm{n}')^{115\mathrm{m}}\mathrm{In}$ system is summarised in the Table 3.12. In comparison to earlier measurements, the current study significantly improved three experimental parameters, including: (1) Choice of suitable monitor reaction: An independent measurements were conducted using a different neutron flux monitor. This helped in the verification of the measured data's consistency with previous measurements, (2) HPGe detector: In comparison to prior measurements, high resolution co-axial HPGe detector with an energy resolution of 1.88 keV at 1332.50 keV gammas of $^{60}\mathrm{Co}$ was used to obtain interference free gamma-ray peaks, (3) Covariance analysis: The ratio technique of covariance analysis has been used to estimate the uncertainty and correlation between the current experimental data which considers the collective uncertainty from all the attributes in the measurement.

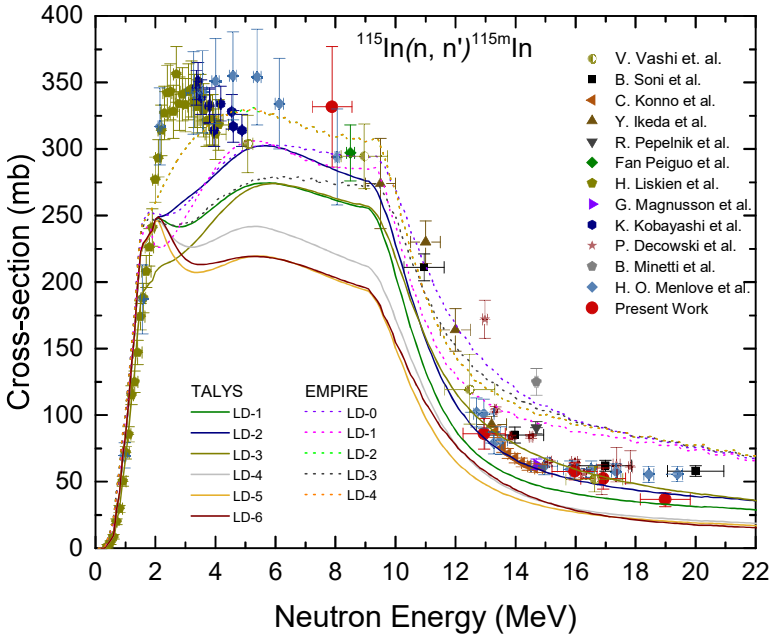

Fig. 3.13: Experimentally measured $^{115}\mathrm{In}(\mathrm{n},\mathrm{n}')^{115\mathrm{m}}\mathrm{In}$ reaction cross-section compared with the literature data and theoretical nuclear models of TALYS-1.95 [14] and EMPIRE-3.2.3 [51].

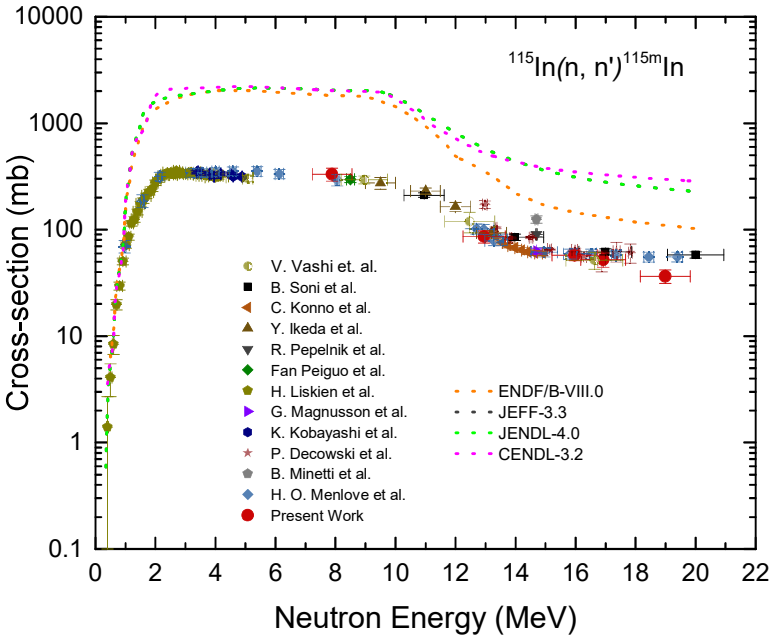

Fig. 3.14: Experimentally measured $^{115}\mathrm{In}(\mathrm{n},\mathrm{n}')^{115\mathrm{m}}\mathrm{In}$ reaction cross-section compared with the literature data and different evaluated data libraries such as ENDF/B-VIII.0[15], JEFF-3.3[16], JENDL-4.0[17] and CENDL-3.2[18].

Table 3.12: Comparison of experimental conditions for $^{115}\mathrm{In}(\mathrm{n},\mathrm{n}')^{115\mathrm{m}}\mathrm{In}$ system[13].

Author (year)	Detector	Monitor reaction	Threshold Energy (MeV)	Covariance analysis	Reference
Hingu et al. (2022)	HPGe	$^{113}\mathrm{In}(\mathrm{n},\mathrm{n}')^{113\mathrm{m}}\mathrm{In}$	0	Yes	Present work
Vashi et al. (2021)	HPGe	$^{232}\mathrm{Th}(\mathrm{n},\mathrm{f})^{97}\mathrm{Zr}$	0	No	[48]
Soni et al. (2020)	HPGe	$^{27}\mathrm{Al}(\mathrm{n},\alpha)^{24}\mathrm{Na}$	3.25	Yes	[59]
Konno et al. (1993)	HPGe	$^{93}\mathrm{Nb}(\mathrm{n},2\mathrm{n})^{92\mathrm{m}}\mathrm{Nb}$	8.93	No	[60]
Ikeda et al. (1992)	HPGe	$^{197}\mathrm{Au}(\mathrm{n},2\mathrm{n})^{196}\mathrm{Au}$	8.12	No	[61]
Pepelnik et al. (1985)	Ge(Li)	$^{27}\mathrm{Al}(\mathrm{n},\alpha)^{24}\mathrm{Na}$	3.25	No	[62]
		$^{26}\mathrm{Mg}(\mathrm{n},\alpha)^{23}\mathrm{Ne}$	5.63		
		$^{27}\mathrm{Al}(\mathrm{n},\mathrm{p})^{27}\mathrm{Mg}$	1.90		
Peiguo et al. (1985)	Nai(Tl) & Ge(Li)	$^{27}\mathrm{Al}(\mathrm{n},\alpha)^{24}\mathrm{Na}$	3.25	No	[63]
Liskien et al. (1978)	Ge(Li)	$^{1}\mathrm{H}(\mathrm{n},\mathrm{n})^{1}\mathrm{H}$	0	No	[64]
Magnusson et al. (1977)	Ge(Li)	$^{27}\mathrm{Al}(\mathrm{n},\alpha)^{24}\mathrm{Na}$	3.25	No	[65]
Koboyashi et al. (1973)	Nai(Tl)	Absolute neutron flux	-	No	[66]
Dekowski et al. (1970)	Scintillation spectrometer	$^{64}\mathrm{Zn}(\mathrm{n},2\mathrm{n})^{63}\mathrm{Zn}$	12.01	No	[67]
Minetti et al. (1968)	NaI(Tl)	$^{3}\mathrm{H}(\mathrm{d},\mathrm{n})^{4}\mathrm{He}$	0	No	[68]
Menlove et al. (1967)	NaI(Tl)	$^{235}\mathrm{U}(\mathrm{n},\mathrm{f})$	0	No	[69]
		$^{27}\mathrm{Al}(\mathrm{n},\alpha)^{24}\mathrm{Na}$	3.25		

3.6.4 Summary and Conclusions

In the present work, the cross-section for the $^{115}\mathrm{In}(\mathrm{n},\mathrm{n}')^{115\mathrm{m}}\mathrm{In}$ reaction was determined at at $7.89 \pm 0.66, 12.95 \pm 0.70, 15.97 \pm 0.75, 16.99 \pm 0.75, 18.99 \pm 0.83$ MeV neutron energies using standard neutron activation analysis and HPGe based γ-ray spectrometry employing a new monitor reaction. The uncertainty calculated using the covariance analysis was found to be in the range of 11-15 %. The present experimental results were compared with the theoretical calculations carried out by using the TALYS and EMPIRE codes, using different LD models prescribed in the respective codes. It may be remarked that, TALYS LD model 2 gives by far the best reproduction of the present experimental results as compared to the other LD models. The EMPIRE model calculations consistently overestimate the experimental results. The current results are additionally compared with the different evaluated data libraries such as ENDF/B-VIII.0, JEFF-3.3, JENDL-4.0, CENDL-3.2 along with literature data. The results of the evaluated data libraries were found to be approximately an order of magnitude higher than the experimental data, likely due to the lack of normalization in evaluated data, whereas the TALYS theoretical data is normalized with experimental data. Thus, experimental data is recommended for accurate flux measurements. The current study adds to the existing data set by employing a new monitor reaction and improving the experimental methods.

✠ ✠ ✠ ✠

References

[1] U. Fischer, P. Batistoni, E. Cheng, et al., in AIP Conference Proceedings, Vol. 769 (American Institute of Physics, 2005), pp. 1478–1485.

[2] C. D. Bowman, Annual Review of Nuclear and Particle Science **48**(1), 505–556 (1998).

[3] A. Gandhi, A. Sharma, A. Kumar, et al., Physical Review C **102**(1), 014603 (2020).

[4] P. Singh, S. Gupta, M. Kansara, et al., Pramana **59**, 739–744 (2002).

[5] S. Santra, K. Mahata, P. Singh, et al., Nuclear Instruments and Methods in Physics Research Section A: Accelerators, Spectrometers, Detectors and Associated Equipment **496**(1), 44–50 (2003).

[6] A. Gupta, P. Bhagwat, and R. Choudhury, Proceedings of HIAT09, Venice, Italy (2009).

[7] https://www.nndc.bnl.gov/nudat/, Accessed: 2022-06-25, 2022.

[8] B. Shivashankar, S. Ganesan, H. Naik, et al., Nuclear Science and Engineering **179**(4), 423–433 (2015).

[9] N. Otuka, B. Lalremruata, M. Khandaker, et al., Radiation Physics and Chemistry **140**, 502–510 (2017).

[10] V. Semkova, V. Avrigeanu, T. Glodariu, et al., Nuclear Physics A **730**(3-4), 255–284 (2004).

[11] C. Whitmarsh (Oak Ridge National Laboratory for the US Atomic Energy Commission, 1962).

[12] D. L. Mollin, Proceedings of the Royal Society of Medicine **55**, 141–145 (1962).

[13] V. Zerkin and B. Pritychenko, Nuclear Instruments and Methods in Physics Research Section A: Accelerators, Spectrometers, Detectors and Associated Equipment **888**, 31–43 (2018).

[14] A. Koning, S. Hilaire, and M. C. Duijvestijn, in International Conference on Nuclear Data for Science and Technology (EDP Sciences, 2007), pp. 211–214.

[15] D. A. Brown, M. Chadwick, R. Capote, et al., Nuclear Data Sheets **148**, 1–142 (2018).

[16] A. J. Plompen, O. Cabellos, C. De Saint Jean, et al., The European Physical Journal A **56**(7), 1–108 (2020).

[17] K. Shibata, O. Iwamoto, T. Nakagawa, et al., Journal of Nuclear Science and Technology **48**(1), 1–30 (2011).

[18] Z. Ge, R. Xu, H. Wu, et al., in EPJ Web of Conferences, Vol. 239 (EDP Sciences, 2020), p. 09001.

[19] R. Pachuau, B. Lalremruata, N. Otuka, et al., Nuclear Science and Engineering **187**(1), 70–80 (2017).

[20] J. Meadows and D. Smith, tech. rep. ANL-7938 (Argonne National Laboratory, Illinois, USA, 1972).

[21] A. Bakshi, S. Dawn, S. Suryanarayana, et al., Nuclear Instruments and Methods in Physics Research Section A: Accelerators, Spectrometers, Detectors and Associated Equipment **949**, 162926 (2020).

[22] L. Punte, B. Lalremruata, N. Otuka, et al., Physical Review C **95**(2), 024619 (2017).

[23] A. Gandhi, A. Sharma, R. Pachuau, et al., The European Physical Journal A **57**(1), 1–12 (2021).

[24] T. Vidmar, Nuclear Instruments and Methods in Physics Research Section A: Accelerators, Spectrometers, Detectors and Associated Equipment **550**(3), 603–608 (2005).

[25] M. Upadhyay, M. Choudhary, N. Singh, et al., Journal of Physics G: Nuclear and Particle Physics **50**(12), 125107 (2023).

[26] A. Trkov, P. J. Griffin, S. Simakov, et al., Nuclear Data Sheets **163**, 1–108 (2020).

[27] A. Hingu, B. Soni, S. Parashari, et al., Radiation Physics and Chemistry **199**, 110270 (2022).

[28] S. Parashari, S. Mukherjee, S. Suryanarayana, et al., Physical Review C **99**(4), 044602 (2019).

[29] D. Millsap and S. Landsberger, Applied Radiation and Isotopes **97**, 21–23 (2015).

[30] Sangeeta, T. Ghosh, B. Maheshwari, et al., Physical Review C **105**, 044320 (2022).

[31] F. S. Chang, J. B. French, and T. H. Thio, Annals of Physics **66**(1), 137–188 (1971).

[32] J. French and K. Ratcliff, Physical Review C **3**(1), 94 (1971).

[33] V. Kota and K. Kar, Pramana **32**, 647–692 (1989).

[34] V. Kota and D. Majumdar, Nuclear Physics A **604**(2), 129–162 (1996).

[35] M. Horoi, J. Kaiser, and V. Zelevinsky, Physical Review C **67**(5), 054309 (2003).

[36] M. Horoi, M. Ghita, and V. Zelevinsky, Physical Review C **69**(4), 041307 (2004).

[37] I. Pasha, B. Rudraswamy, Y. Sheela, et al., Journal of High Energy Physics (2020).

[38] S. Parashari, S. Mukherjee, H. Naik, et al., The European Physical Journal A **55**(4), 1–16 (2019).

[39] A. A. Filatenkov, tech. rep. INDC (CCP)-0460 (International Atomic Energy Agency (IAEA), 2016).

[40] B. Shivashankar, H. Naik, S. Suryanarayana, et al., Journal of Radioanalytical and Nuclear Chemistry **292**(2), 745–750 (2012).

[41] F. Zhou, X. Xiao, K. Fang, et al., Nuclear Instruments and Methods in Physics Research Section B: Beam Interactions with Materials and Atoms **269**(7), 642–646 (2011).

[42] W. Mannhart and D. Schmidt, tech. rep. (Karlsruhe Institute of Technology, 2007).

[43] A. Harun-Ar-Rashid, M. Khandaker, M. Islam, et al., Indian Journal of Physics **80**, 737–743 (2006).

[44] M. Bhike, A. Saxena, B. K. Nayak, et al., in Proceedings of the DAE-BRNS Symposium on Nuclear Physics, Vol. 51, edited by S. Kailas, S. Kumar, and S. Santra (2006).

[45] T. Shimizu, H. Sakane, M. Shibata, et al., Annals of Nuclear Energy **31**(9), 975–990 (2004).

[46] T. Senga, H. Sakane, M. Shibata, et al., tech. rep. (Japan Atomic Energy Research Institute, 2000).

[47] D. A. Petti, tech. rep. (EG and G Idaho, Inc., Idaho Falls, USA, 1987).

[48] V. Vashi, R. Makwana, S. Mukherjee, et al., The European Physical Journal Plus **136**(7), 1–12 (2021).

[49] V. Zerkin and B. Pritychenko, Nuclear Instruments and Methods in Physics Research Section A: Accelerators, Spectrometers, Detectors and Associated Equipment **888**, 31–43 (2018).

[50] A. Koning, S. Hilaire, and M. Duijvestijn, NRG-1755 ZG Petten, The Netherlands (2019).

[51] M. Herman, R. Capote, B. Carlson, et al., Nuclear data sheets **108**(12), 2655–2715 (2007).

[52] J. F. Ziegler, M. D. Ziegler, and J. P. Biersack, Nuclear Instruments and Methods in Physics Research Section B: Beam Interactions with Materials and Atoms **268**(11-12), 1818–1823 (2010).

[53] C. Poppe, J. Anderson, J. Davis, et al., Physical Review C **14**(2), 438 (1976).

[54] S. Mashnik, M. Chadwick, H. Hughes, et al., arXiv preprint nucl-th/0011066 (2000).

[55] R. Makwana, S. Mukherjee, P. Mishra, et al., Physical Review C **96**(2), 024608 (2017).

[56] A. Chatterjee, A. Kumar, and K. Ramachandran, in Proceedings of the DAE-BRNS Symposium on Nuclear Physics, Vol. 55 (Board of Research in Nuclear Sciences (BRNS), Department of Atomic Energy (DAE), 2010), pp. 756–757.

[57] C. Midhun, M. Musthafa, S. Suryanarayana, et al., Physical Review C **104**(5), 054606 (2021).

[58] D. Smith, A. Plompen, and V. Semkova, Neutron Activation Cross-Section Measurements from Threshold to **20** (2005).

[59] B. Soni, S. Parashari, S. Mukherjee, et al., The European Physical Journal Plus **135**(3), 1–21 (2020).

[60] C. Konno, Y. Ikeda, K. Oishi, et al., JAERI reports 1329 (1993).

[61] Y. Ikeda, C. Konno, M. Mizumoto, et al., in Nuclear Data for Science and Technology (Springer, 1992), pp. 294–296.

[62] R. Pepelnik, B. Anders, B. Banal, et al., Report: GKSS in Progress Report on Nuclear Data Research in Germany, vol 1984 (1985).

[63] F. Peiguo, Z. Wenrong, T. Dan, et al., Zhonghua Heyixue Zazhi;(China) **7**(3) (1985).

[64] H. Liskien, F. Arnotte, R. Widera, et al., Nuclear Science and Engineering **67**(3), 334–338 (1978).

[65] G. Magnusson and I. Bergqvist, Nuclear Technology **34**(1), 114–121 (1977).

[66] K. Kobayashi, I. Kimura, H. Gotoh, et al., Journal of Nuclear Energy **27**(10), 741–745 (1973).

[67] P. Decowski, W. Grochulski, J. Karolyi, et al., Swierk+Warsaw, Repts, No. 1197 (1197), 18 (1970).

[68] B. Minetti and A. Pasquarelli, Zeitschrift für Physik A Hadrons and nuclei **217**(1), 83–90 (1968).

[69] H. Menlove, K. Coop, H. Grench, et al., Physical Review **163**(4), 1308 (1967).